# Simulation Of Electromagnetic Scattering Experiments In The NSWC Carderock MASK Facility

**Robert J. Burkholder and Khalid Jamil**

The Ohio State University

## ElectroScience Laboratory

Department of Electrical Engineering
1320 Kinnear Road
Columbus, Ohio  43212

20030422 043

5027272-101

| REPORT DOCUMENTATION PAGE | 1. REPORT NO. | 2. | 3. Recipient's Accession No. |
|---|---|---|---|
| **4. Title and Subtitle** Simulation of Electromagnetic Scattering Experiments in the NSWC Carderock MASK Facility | | | **5. Report Date** February 2003 |
| | | | **6.** |
| **7. Author(s)** Robert J. Burkholder and Khalid Jamil | | | **8. Performing Org. Rept. No.** 742962-1 |
| **9. Performing Organization Name and Address** **The Ohio State University** **ElectroScience Laboratory** **1320 Kinnear Road** **Columbus, OH 43212** | | | **10. Project/Task/Work Unit No.** |
| | | | **11. Contract (C) or Grant (G) No.** (C) N00014-02-1-0727 |
| **12. Sponsoring Organization Name and Address** Office of Naval Research Program Officer: Ronald P. Radlinski Ballston Centre Tower One 800 N.Quincy Street Arlington, VA 2217-5600 | | | **13. Report Type/Period Covered** Report |
| | | | **14.** |

**15. Supplementary Notes**

**16. Abstract (Limit: 200 words)**

Radar scattering experiments performed in the NSWC Carderock Maneuvering And Sea-Keeping (MASK) wavetank facility are simulated using computational and analytic solutions. Forward scattering over a rough sea surface is simulated, as well as the backscatter from plate targets suspended over the rough surface. The generalized forward backward method is used to simulate the measurements with a 2D model, and a reduced order iterative physical optics method is used for a 3D model. Monte Carlo data sets for multiple surface realizations are generated to extract the coherent and incoherent scattering from the computer simulations.

**17. Document Analysis**

**a. Descriptors** Sea surface, Electromagnetic scattering, Rough Surfaces, Radar cross sections, Numerical analysis, Monte Carlo methods, Integral equations, Physical optics, radar measurements

**b. Identifiers/Open-Ended Terms**

**c. COSATI Field/Group**

| 18. Availability Statement | 19. Security Class (This report) Unclassified | 21. No. of Pages 59 |
|---|---|---|
| Approved for public release; Distribution is unlimited. | 20. Security Class (This page) Unclassified | 22. Price |

(See ANSI-Z39.18)     *See Instructions on Reverse*     OPTIONAL FORM 272(4-77)
Department of Commerce

# Acknowledgments

# Contents

# List of Figures

# List of Tables

# Chapter 1

# Introduction

This report describes the computer simulation of scattering measurements performed inside the NSWC Carderock Maneuvering And SeaKeeping (MASK) facility. The MASK facility has a large wave tank for generating scaled ocean surfaces as a function of sea state. The scattering measurements performed in the MASK facility are to be used to study the effect of the rough ocean surface on the propagation and scattering of low-angle radar signals. They are also to provide experimental validation for computer and analytic models, such as those developed under ONR grant N00014-98-1-0243 reported in [1, 2, 3].

Figure 1.1 shows the experimental set-up for the forward scatter and backscatter measurements. In the forward scatter measurements a transmitting antenna (Tx) illuminates the sea surface, and a receiving antenna measures the incident and sea scattered fields. In the backscatter measurements the transmitting antenna illuminates the sea surface and a target on or above the surface, and a co-located receiving antenna measures the backscatter. The target simulated in this report is a flat plate suspended above the surface, which may rotate on an axis transverse to the incident beam direction. The rough sea surface is created by the MASK wave maker for a desired wave spectrum within a given sea state. The measurements encompass a variety of antenna heights and sea states as described in Chapter 2, and are obtained over a band of frequencies for each measurements. The experiment is designed to simulate an L-band radar over a realistic ocean by scaling the frequencies, ocean spectra, and physical dimensions to an equivalent 1/10 scale model at X-band. This scaling and
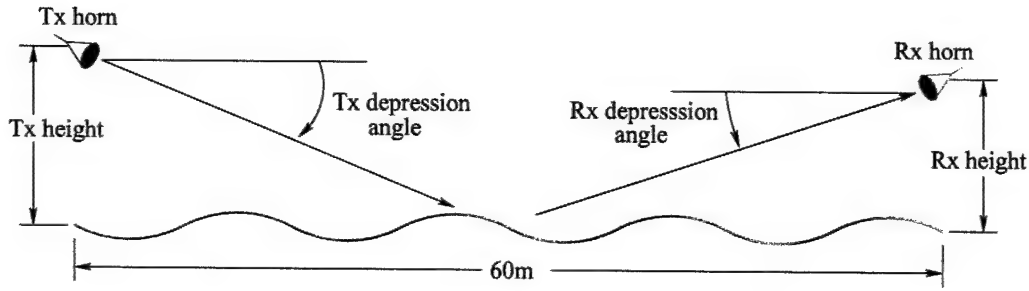
(a) Forward scatter experimental set-up.
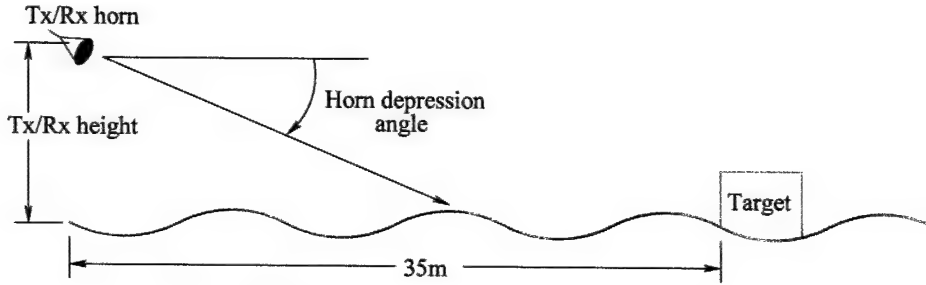


(a) Backscatter experimental set-up.

Figure 1.1: Experimental set-ups for forward and backscatter measurements over a rough sea surface.

experimental set-up is discussed in detail in Chapter 2.

The measurements are simulated here using the computational methods developed in [1, 2, 3], namely, the generalized forward-backward (GFB) method [4, 5] and the forward-backward iterative physical optics (FBIPO) method [6, 7, 8].

## 1.1 The Generalized Forward-Backward Method

The GFB method was developed for two-dimensional geometries involving a target on or above a very long rough surface, as illustrated in Figure 1.2. It is a numerically rigorous method of moments (MoM) solution that is solved iteratively by taking advantage of the forward and backward nature of the propagation over a long rough surface. The forward-backward iteration makes the solution converge in only a few cycles. The GFB is a generalization of the forward-backward method [9], or equivalently, the method of ordered multiple interactions [10], which were developed for single-valued rough surfaces without a target
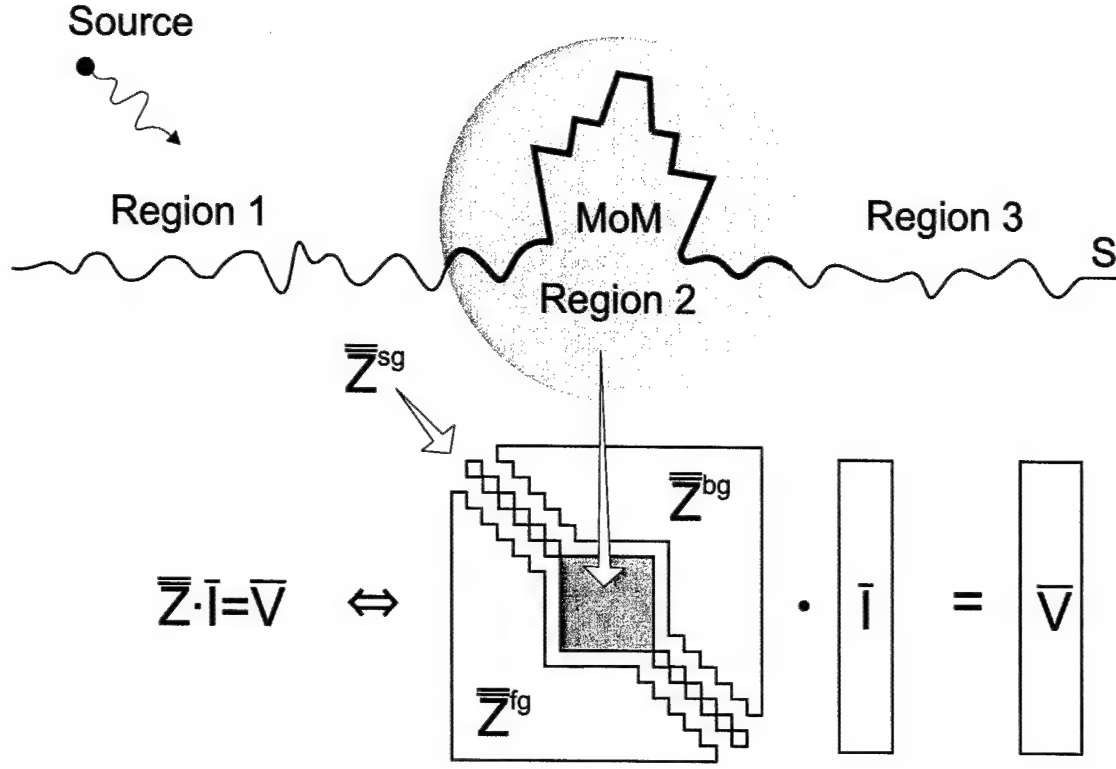
Figure 1.2: Matrix decomposition used in the generalized forward-backward method. The Region 2 matrix is solved directly within the forward-backward iteration process.

present. The GFB method isolates the portion of the MoM matrix associated with the target region, and solves it directly within the forward-backward iteration process. Figure 1.2 shows the matrix decomposition used in the GFB solution. The efficiency of the GFB method is remarkably improved by adapting the spectral acceleration approach of [11]. This work is described in [1] and [12].

The only limitation of the GFB method is it is restricted to 2D geometries. Also, note that the infinite sea surface must be artificially truncated to apply the MoM solution. To reduce the effects of the endpoint truncation, tapered R-card material is attached to both ends of the sea surface as described in [12]. Comparison with infinite surface reference solutions shows that this approach provides excellent accuracy. The majority of the simulations reported here are obtained with the GFB method.
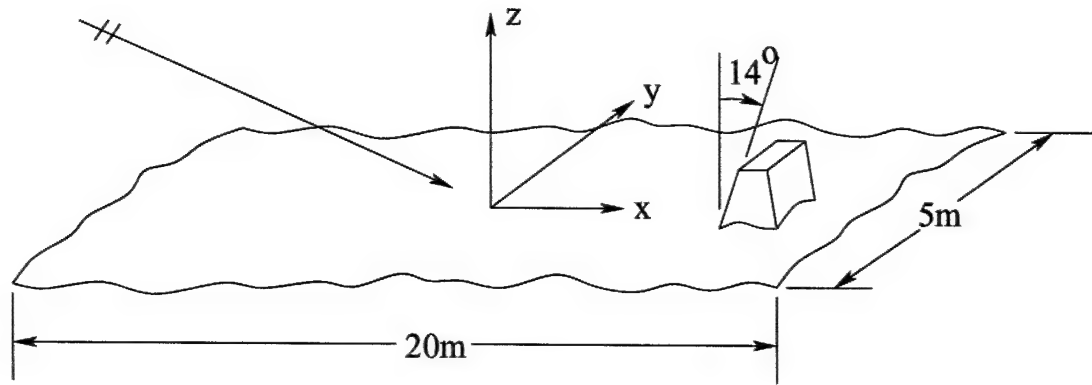
Figure 1.3: 3D target on a rough sea surface analyzed using the forward-backward iterative physical optics method.

## 1.2 The Forward-Backward Iterative Physical Optics Method

The basic IPO method for computing the scattering from arbitrary three-dimensional geometries starts with the first-order PO currents on the exposed surfaces and allows them to re-radiate iteratively until a converged solution is obtained [8]. It was originally developed for computing the scattering from large open cavities [6]. The multiple iterations take into account the many multiple reflections and diffractions that occur within cavities and other multibounce geometries. The forward-backward IPO adapts the same principle of forward-backward propagation to greatly improve the convergence of the IPO method [7]. The numerical PO integration is accelerated using the fast far-field approximation as described in [13].

In [3], the FBIPO method is applied to the scattering from 3D targets on rough sea surfaces such as shown in Figure 1.3. Again, the sea surface must be artificially truncated to allow the application of the numerical model. However, instead of using R-cards to eliminate the truncation edge scattering effects, endpoint subtraction is used. Since we are interested in computing the scattering due to the presence of the target, we can subtract the scattering from the sea surface with the target absent from the total scattering with the target present. This provides very good accuracy compared with an infinite surface reference

4

solution, although the subtraction also removes the surface clutter component which may be significant.

### 1.2.1 Reduced Order Iterative Physical Optics Method

As will become clear in subsequent chapters, the area of sea surface illuminated by the incident radar beam requires millions of PO sample points at X-band. This is intractably large for the FBIPO method in its basic form because each point radiates to all other points. To ease the computational burden, a reduced order IPO method is introduced here. This method ignores the surface-to-surface interactions, which dominate the computational burden because the illuminated surface is much larger than the target. The reduced IPO iterates on the surface-target and target-target interactions. Therefore, each sample point on the surface only radiates to points on the target, and vice versa. Points on the target also radiate to other points on the target, but this requires a relatively small amount of CPU time because the target is much smaller than the surface.

The reduced order PO method reduces to first order PO when the target is absent, as in the case of the forward scattering simulations of Chapter 3, or when the subtraction method is used to remove the surface truncation effects from the backscatter simulations of Chapter 4.

## 1.3 Organization of Report

Chapter 2 describes the experimental set-up and parameters used in the NSWC Carderock MASK facility, as well as descriptions of the hydrodynamics and material modeling used in the simulations. The Monte Carlo statistical processing is also discussed. Chapter 3 presents the results of the simulations of the forward scattering measurements, and Chapter 4 presents the results for the backscatter simulations. Finally, Chapter 5 discusses the findings of the simulation study, and suggests future work.

# Chapter 2

# Experimental Set-Up

In the forward scatter measurements, a transmitting antenna (Tx) illuminates the sea surface at a low elevation angle and the received signal is measured at the receiving antenna (Rx), as shown in Figure 1.1(a). The horizontal range from the transmitter to the receiver is 60 m. The transmitter and receiver may move vertically. In the backscatter measurements, a transmit/receiver antenna (Tx/Rx) illuminates a target on or over the sea surface and the backscattered signal is measured, as shown in Figure 1.1(b). The horizontal range from the transmitter to the receiver is 35 m, although the range may vary slightly for different targets. The transmitter/receiver may move vertically.

For both forward and backscatter measurements, the received signal is measured from 8 to 12 GHz as a function of the wave state generated in the NSWC Carderock MASK facility. The measurements are designed to simulate the scattering over a rough ocean surface in the 0.8 to 1.2 GHz frequency band, so the frequency is scaled by 10 and the physical dimensions and wave spectra are scaled by 1/10 in the MASK facility.

## 2.1 Antenna Locations and Orientations

The transmit (Tx) and receive (Rx) antennas used in the measurements are identical corrugated conical horns with aperture diameter 0.146 m and flare angle approximately 25°. The half-power beamwidth is approximately 20°. Table 2.1 lists the vertical positions and orientations (depression angles) of the horn antennas used for the forward scattering mea-

6

surements. The measurements included all combinations of Tx and Rx heights, while the simulations presented in the next chapter include only the three combinations listed in Table 2.1. This is a result of the large amount of CPU time required for each Monte Carlo simulation. Table 2.2 gives the positions and orientations of the transmit/receive antenna used for the backscatter measurements. The simulations use only the highest Tx/Rx height.

|   | Tx height (m) | Tx dep. angle | Rx height (m) | Rx dep. angle |
|---|---|---|---|---|
| 1 | 1.05 | 2.0° | 0.75 | 3° |
| 2 | 3.14 | 6.0° | 1.25 | 3° |
| 3 | 5.25 | 9.9° | 1.75 | 3° |

Table 2.1: Vertical positions and orientations (depression angles) of the horn antennas for the forward scattering measurements.

|   | Tx height (m) | Tx dep. angle |
|---|---|---|
| 1 | 1.89 | 6.0° |
| 2 | 3.15 | 9.9° |

Table 2.2: Vertical positions and orientations (depression angle) of the transmit/receive horn antenna for the backscatter measurements.

## 2.2    Targets for Backscatter Measurement

The targets used in the backscatter measurements are a suspended sphere, a suspended rotating flat plate and dihedral, and a floating squat cylinder. The flat plate and dihedral rotate about a horizontal axis transverse to the incident beam. Only the flat plate is simulated here in Chapter 4. This is because the flat plate is the only target that is translationally invariant in the cross-direction, which is necessary for the 2D GFB model to be applicable. Furthermore, the floating squat cylinder moves with the waves, so the existing computer codes need to be significantly modified to model a moving target. It is planned to simulate the sphere, dihedral, and floating cylinder as part of the continuation of this effort.
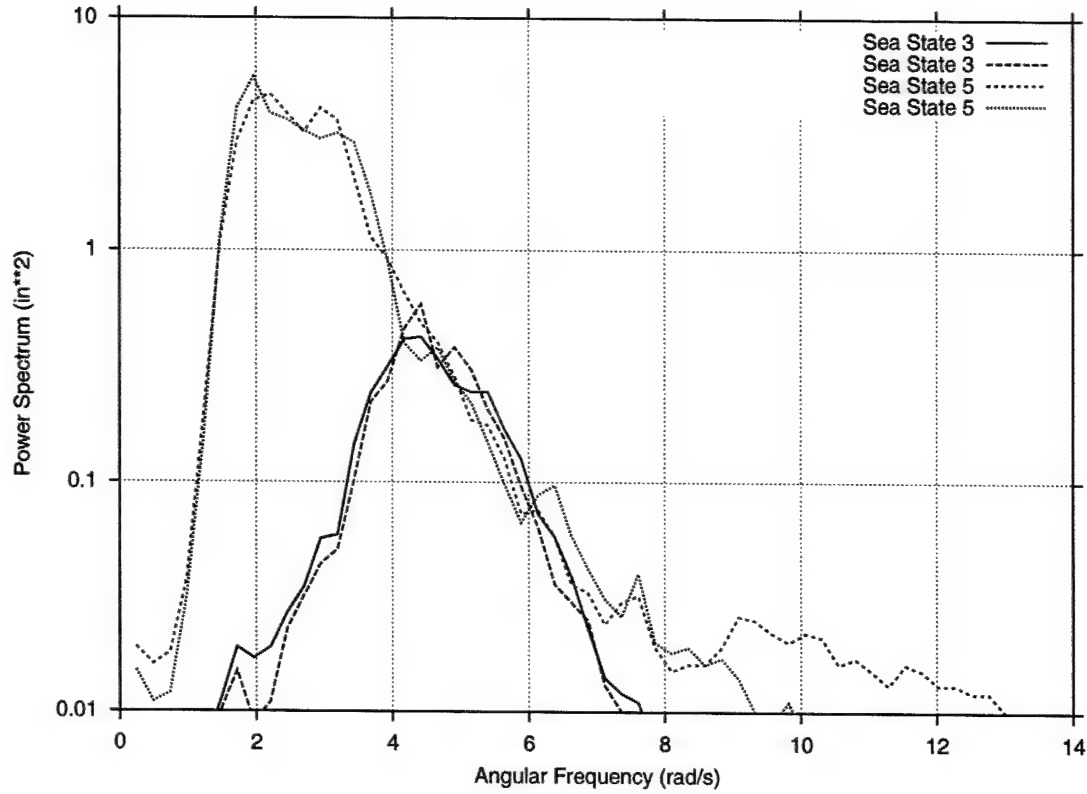
Figure 2.1: Experimental sea spectra for the 1/10 scale Pierson-Moskowitz ocean simulations.

## 2.3 Hydrodynamics

The rough sea surface is generated in the MASK facility with a wave maker that produces an approximate Pierson-Moskowitz ocean spectrum [14]. The spectrum is appropriately modified to simulate an ocean surface at 1/10 scale for various sea states. Figure 2.1 plots the actual measured wave spectra for scaled simulations of sea states 3 and 5. As the figure shows, the spectra have similar features to Pierson-Moskowitz spectra, i.e., a higher sea state gives rise to larger, longer ocean waves. The measured spectra are given as a function of the angular frequency $\omega$ of the ocean waves, which is related to the wavenumber $K$ by the dispersion relation $\omega = \sqrt{gK}$, where $g = 9.81$ m/s is the gravitational acceleration constant at sea level [15].

Table 2.3 gives the sea states and wave heights of the ocean surfaces simulated in the measurements, where $H_{1/3}$ is the average *significant wave height* for each sea state [15]. The

8

| Sea state | $H_{1/3}$ | 1/10 $H_{1/3}$ | 1/10 RMS | Measured RMS |
|---|---|---|---|---|
| 3 | 0.87 | 0.087 | 0.029 | 0.023 |
| 5 | 3.25 | 0.325 | 0.108 | 0.074 |

Table 2.3: Wave heights for sea states 3 and 5 (in meters). $H_{1/3}$ is the average significant wave height for each sea state.

RMS wave height is approximately one-third of $H_{1/3}$. Table 2.3 gives the average scaled RMS wave heights and the actual measured RMS wave heights. It is seen that the measured wave heights are slightly lower than expected for each sea state.

The computer simulations use a pure Pierson-Moskowitz ocean spectrum adjusted to give the same RMS wave height as the measurements. In the simulations the ocean surface is also scaled by a factor of 1/10 with respect to the full scale ocean spectrum.

## 2.4 Material Characterization of Sea Water

The dielectric permittivity $\epsilon$ and magnetic permeability $\mu$ of the sea water are given by

$$\epsilon = (\epsilon' - j\epsilon'')\epsilon_o - j\frac{\sigma_c}{\omega}$$
$$\mu = \mu_o \tag{2.1}$$

where $\mu_o = 4\pi \times 10^{-7}$ h/m and $\epsilon_o = 8.854 \times 10^{-12}$ f/m are the permeability and permittivity of free space, respectively, $\sigma_c = 4$ mho/m is the conductivity of sea water, and $\omega$ is the radian frequency of the time-harmonic electromagnetic field. At a frequency of 10 GHz and temperature 25°C, $\epsilon' = 55$, $\epsilon'' = 30$ [16], so $\epsilon = (55 - j37)\epsilon_o$, which are the parameters used here in the computer models. While the water in the MASK tank does not have as high salinity as sea water, it is expected to have a comparable conductivity due to other dissolved minerals in the water.

The surface integral equation approaches used here model the sea surface as an impenetrable impedance surface with surface impedance given by

$$Z_s = \sqrt{\frac{\mu_o}{\epsilon}}. \tag{2.2}$$

9

For such a high dielectric constant and loss tangent, the impenetrable surface impedance model is very accurate for all angles of incidence in the 8-12 GHz frequency band.

## 2.5 Statistical Processing

Because the computer simulations cannot exactly reproduce the time-varying wave surface in the MASK tank, statistical processing of the data is necessary to obtain a valid comparison between measurements and calculations. The statistical quantities of interest are the coherent and incoherent power at the receiver, defined in terms of the normalized electric field $\tilde{E}$ as

$$\text{Coherent Power} \;=\; |<\tilde{E}>|^2$$
$$\text{Incoherent Power} \;=\; <|\tilde{E}-<\tilde{E}>|^2> \;=\; <|\tilde{E}|^2> - |<\tilde{E}>|^2 \tag{2.3}$$

where $< \cdot >$ denotes the expected value computed over the entire sample for a given frequency, sea state, and antenna configuration. The coherent power depends on the phase of the received field, and is a measure of the power in the time-averaged field at the receiver. The incoherent power is a measure of the variation in the signal due to the time-varying environment. The normalized electric field is defined differently for the forward and backscatter measurements, and will be addressed in Chapters 3 and 4, respectively.

In addition to the coherent and incoherent power, the probability density function (PDF) of the forward scatter simulations is plotted in Chapter 3. A Rice PDF is assumed because the received field has the form of a signal present with noise [17]. It is given by

$$\text{PDF}(|\tilde{E}|) \;=\; \frac{|\tilde{E}|}{\sigma^2} \exp\left(-\frac{|\tilde{E}|^2 + A^2}{2\sigma^2}\right) I_o\left(\frac{|\tilde{E}|A}{\sigma^2}\right) \tag{2.4}$$

where $\sigma$ is the standard deviation, $I_o(\cdot)$ is the modified Bessel function of zero order, and $A = \sqrt{<|\tilde{E}|^2>}$. Note that this PDF is for the magnitude of the normalized received field $|\tilde{E}|$ so it may be plotted on the same dB scale as the coherent and incoherent power. It may be shown that this PDF becomes Gaussian with mean $A$ for $|\tilde{E}|A/\sigma^2 \gg 1$.

Monte Carlo numerical simulations are used in the following chapters to obtain the statistical data. For most of the simulations, 16 samples are used for each data set. This is a

10

relatively small number of samples due to the amount of computer time needed to generate each sample. Convergence tests show that 16 samples gives a result within about 1 dB of the converged Monte Carlo result obtained using a much larger number of samples.

# Chapter 3

# Forward Scatter Simulations

The forward scatter experimental set-up is shown again here in Figure 3.1. The incident radar beam illuminates the sea surface and receiving antenna. The receiving antenna picks up the incident field plus the sea scattered field. The received field normalized to the incident field is computed in the computer simulations, and is defined by

$$\tilde{E} = \frac{E^i + E^s}{E^i} \tag{3.1}$$

where $E^i$ and $E^s$ are the incident (free space) and sea scattered fields, respectively. The incident field is given analytically in the simulations, but is obtained in the measurements by placing an absorbing blocker on the sea surface to eliminate the sea scattered field. The forward backward method (2D) and the physical optics method (3D) are used here to simulate the forward scatter measurements. 16 samples are used in each Monte Carlo simulation from 8-12 GHz.
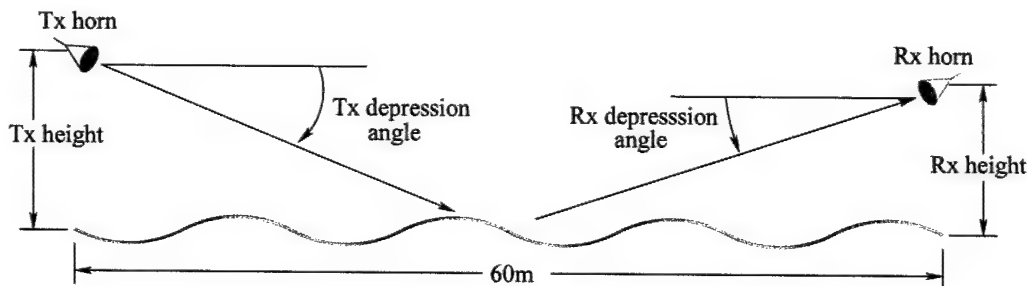


Figure 3.1: Experimental set-up for forward scatter measurements over a rough sea surface.

## 3.1 2D Model using the Forward Backward Method

The generalized forward-backward (GFB) method briefly described in Section 1.1 for 2D geometries reduces to the forward-backward method when no target is present. The normalization defined in (3.1) is approximately independent of whether the solution is 2D or 3D because the spread factor cancels out of the equation.
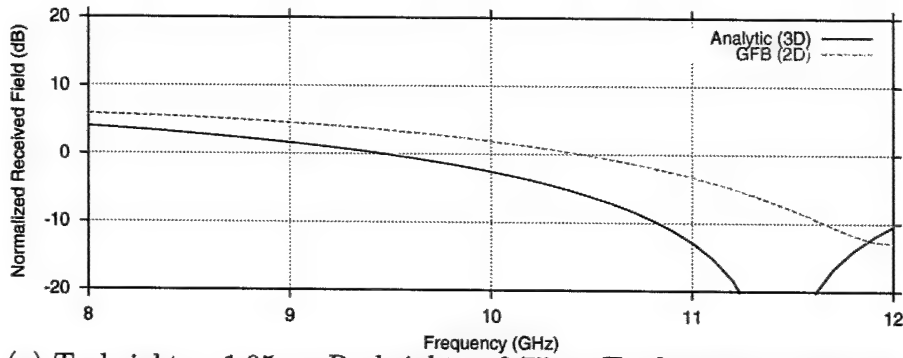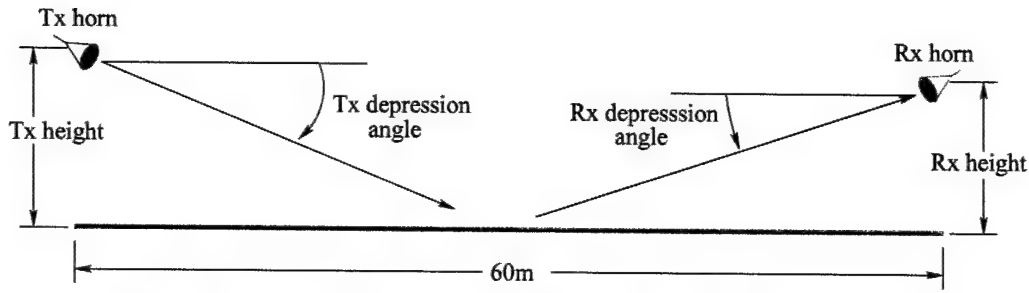
### 3.1.1 Forward Scatter Reference Solution

Before presenting the Monte Carlo data generated by the GFB code, the forward scatter numerical simulations for a flat sea surface are compared here with an analytic solution based on image theory. This solution is obtained by finding the incident and reflected (image) fields via geometrical optics. The sea-reflected field is modified by the appropriate plane wave reflection coefficient for sea water given by

$$R_h(\theta^i) = \frac{Z_s \cos \theta^i - 1}{Z_s \cos \theta^i + 1} \; ; \; R_v(\theta^i) = \frac{\cos \theta^i - Z_s}{\cos \theta^i + Z_s} \tag{3.2}$$

where $R_h$ is for horizontal polarization (H-pol) and $R_v$ is for vertical polarization (V-pol), and $\theta^i$ is the incidence angle measured from the surface normal. It is noted the reference solution is for 3D.

Figures 3.2 and 3.3 show the analytic comparisons with the GFB method. The comparisons are all in very close agreement, except in Figure 3.2(a) which does not show the nulls matching up for H-pol. However, it was found that the position of the null is very sensitive to the exact horn location, so it is possible the GFB computer code did not use exactly the same horn positions as the reference solution.

(a) Tx height = 1.05 m, Rx height = 0.75 m, Tx depression angle 2°.
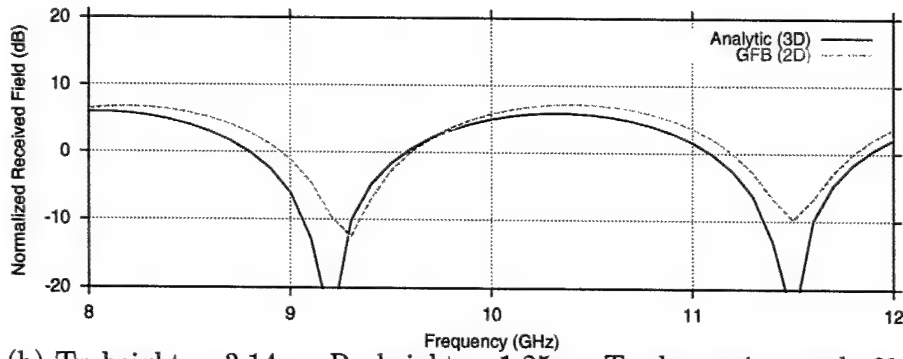
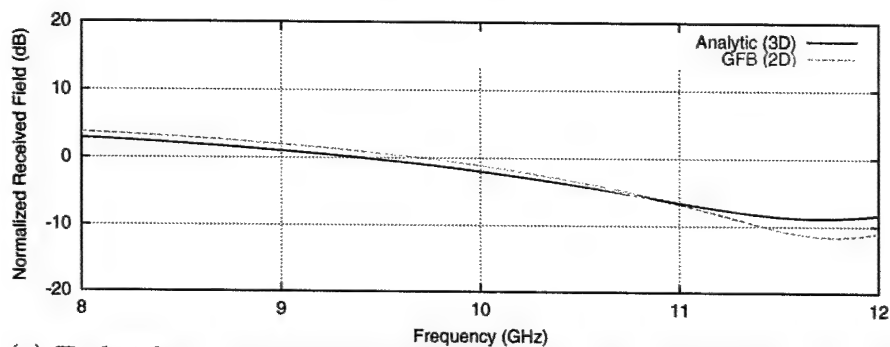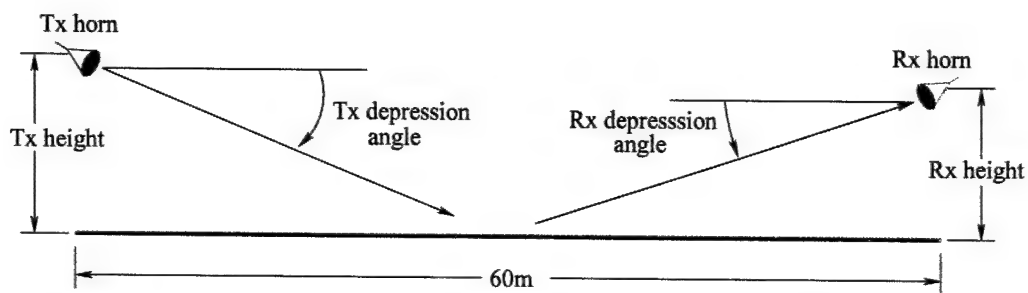(b) Tx height = 3.14 m, Rx height = 1.25 m, Tx depression angle 6°.
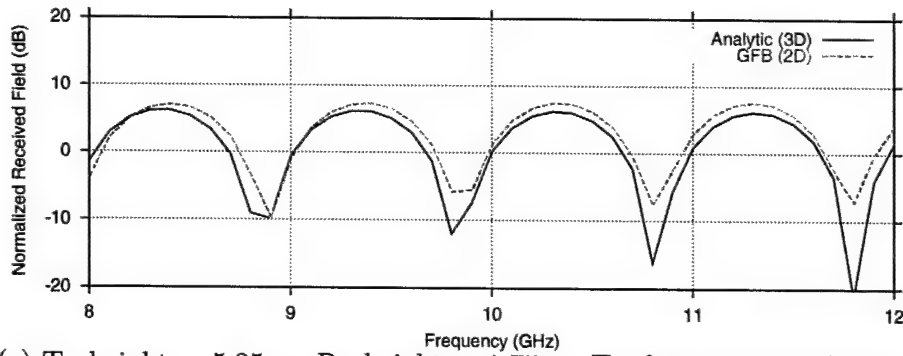
(c) Tx height = 5.25 m, Rx height = 1.75 m, Tx depression angle 9.9°.

Figure 3.2: Analytic reference solution comparisons for flat surface forward scattering, horizontal polarization.

(a) Tx height = 1.05 m, Rx height = 0.75 m, Tx depression angle 2°.



(b) Tx height = 3.14 m, Rx height = 1.25 m, Tx depression angle 6°.


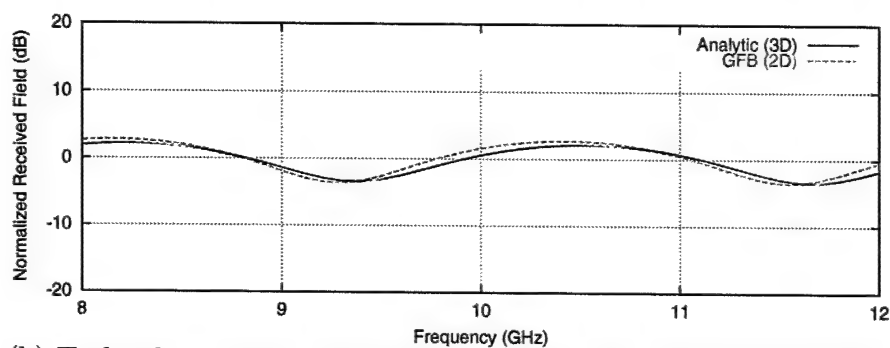
(c) Tx height = 5.25 m, Rx height = 1.75 m, Tx depression angle 9.9°.

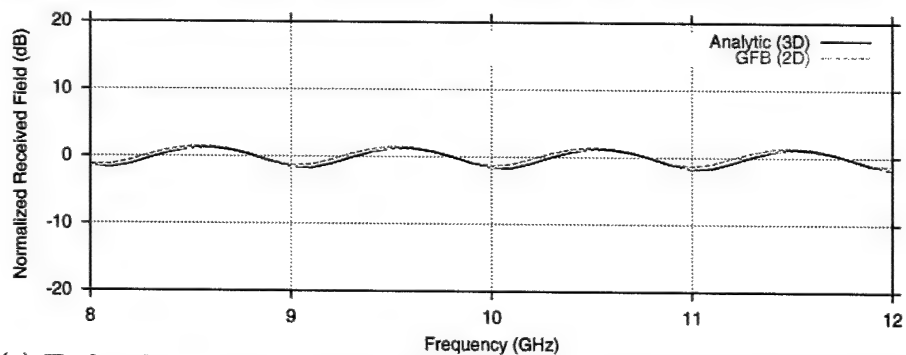Figure 3.3: Analytic reference solution comparisons for flat surface forward scattering, vertical polarization.

15

## 3.1.2  2D Forward Scatter Data

Figures 3.4, 3.5, and 3.6 show color contour plots of the Monte Carlo normalized field data for the three positions of the transmit and receive horns, from lowest position to highest. Sea states 0 (flat surface), 3 and 5 are plotted as a function of frequency from 8-12 GHz, for horizontal and vertical polarization. The color units are in dB relative to the incident field magnitude.

As expected, the data displays more variations for higher seas. The general trend is that higher sea states and higher horn positions show more variations in the fields (i.e., less coherence). The higher horn positions are expected to be more incoherent because it is known that the forward scattered field becomes more coherent for low grazing angles [18]. The V-pol cases show somewhat less variation because the sea surface reflection coefficient is significantly lower than for H-pol near the Brewster angle, which is around 5° elevation. Therefore, the received field is dominated by the incident field for V-pol, which is why the results are all close to 0 dB.

16

Figure 3.4: Contour plots of the forward scatter Monte Carlo data for sea states 3 and 5. Tx height = 1.05 m, Rx height = 0.75 m, Tx depression angle 2°. Color scales in dB.

Figure 3.4: (cont'd.) Contour plots of the forward scatter Monte Carlo data for sea states 3 and 5. Tx height = 1.05 m, Rx height = 0.75 m, Tx depression angle 2°. Color scales in dB.

Figure 3.5: Contour plots of the forward scatter Monte Carlo data for sea states 3 and 5. Tx height = 3.14 m, Rx height = 1.25 m, Tx depression angle 6°. Color scales in dB.

Figure 3.5: (cont'd.) Contour plots of the forward scatter Monte Carlo data for sea states 3 and 5. Tx height = 3.14 m, Rx height = 1.25 m, Tx depression angle 6°. Color scales in dB.
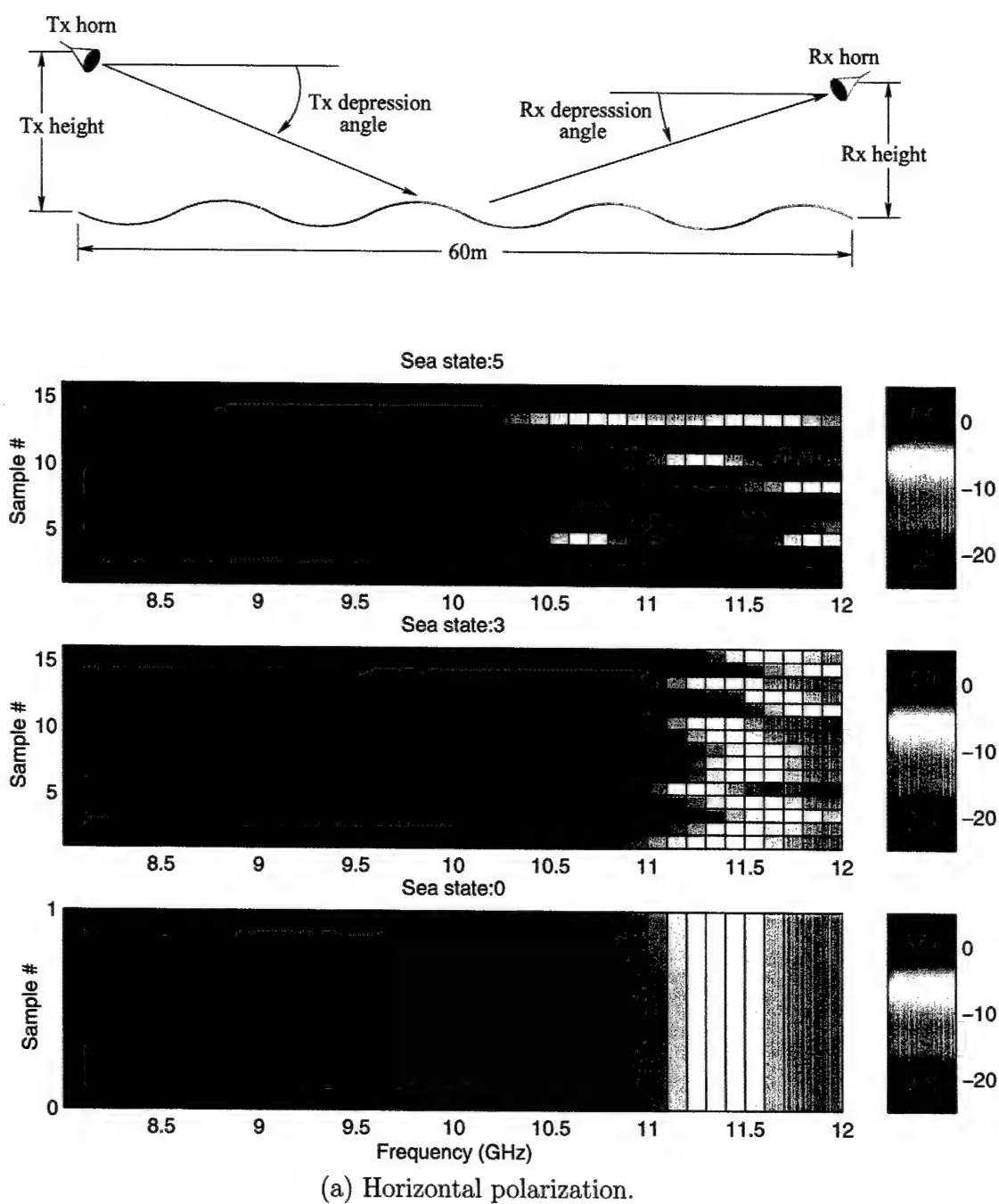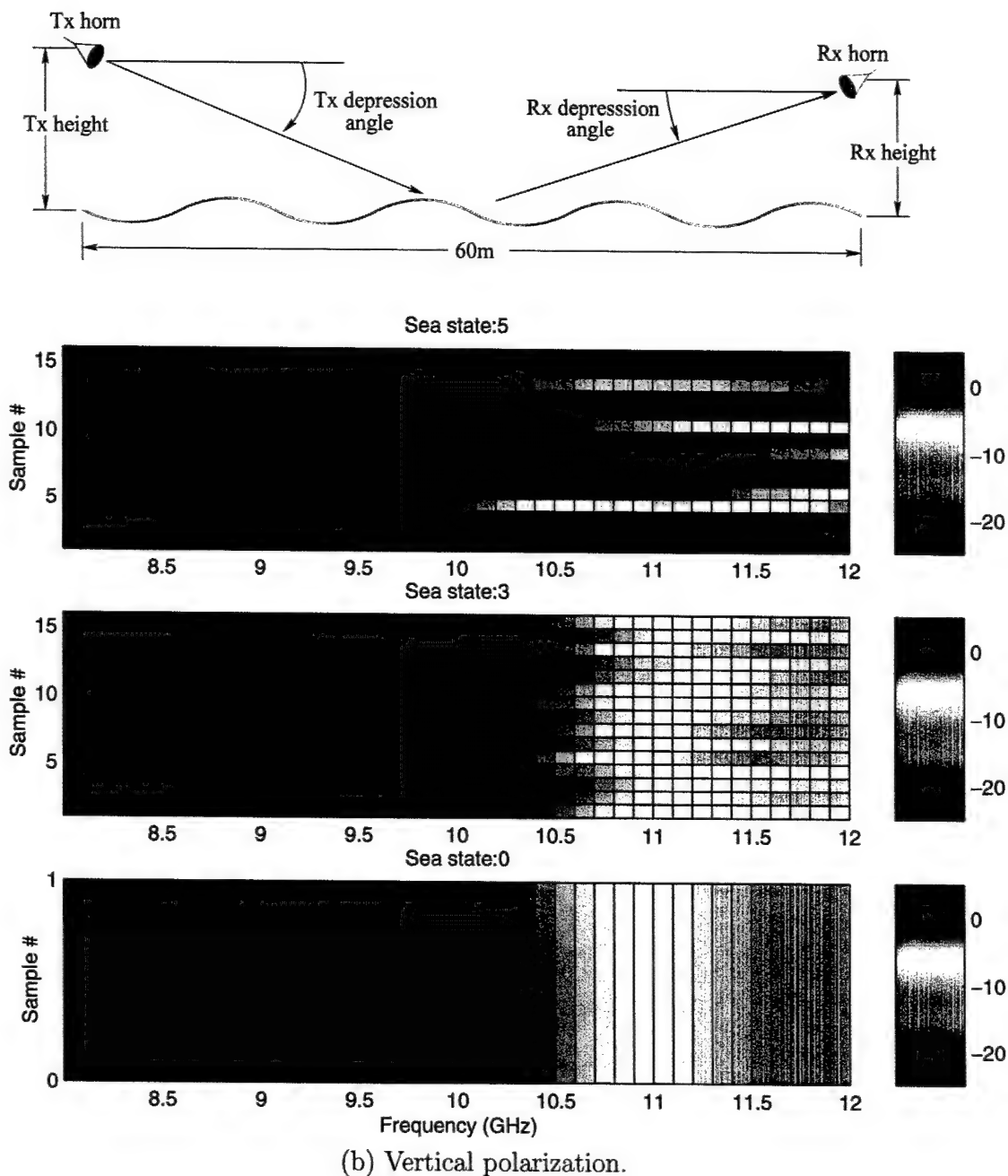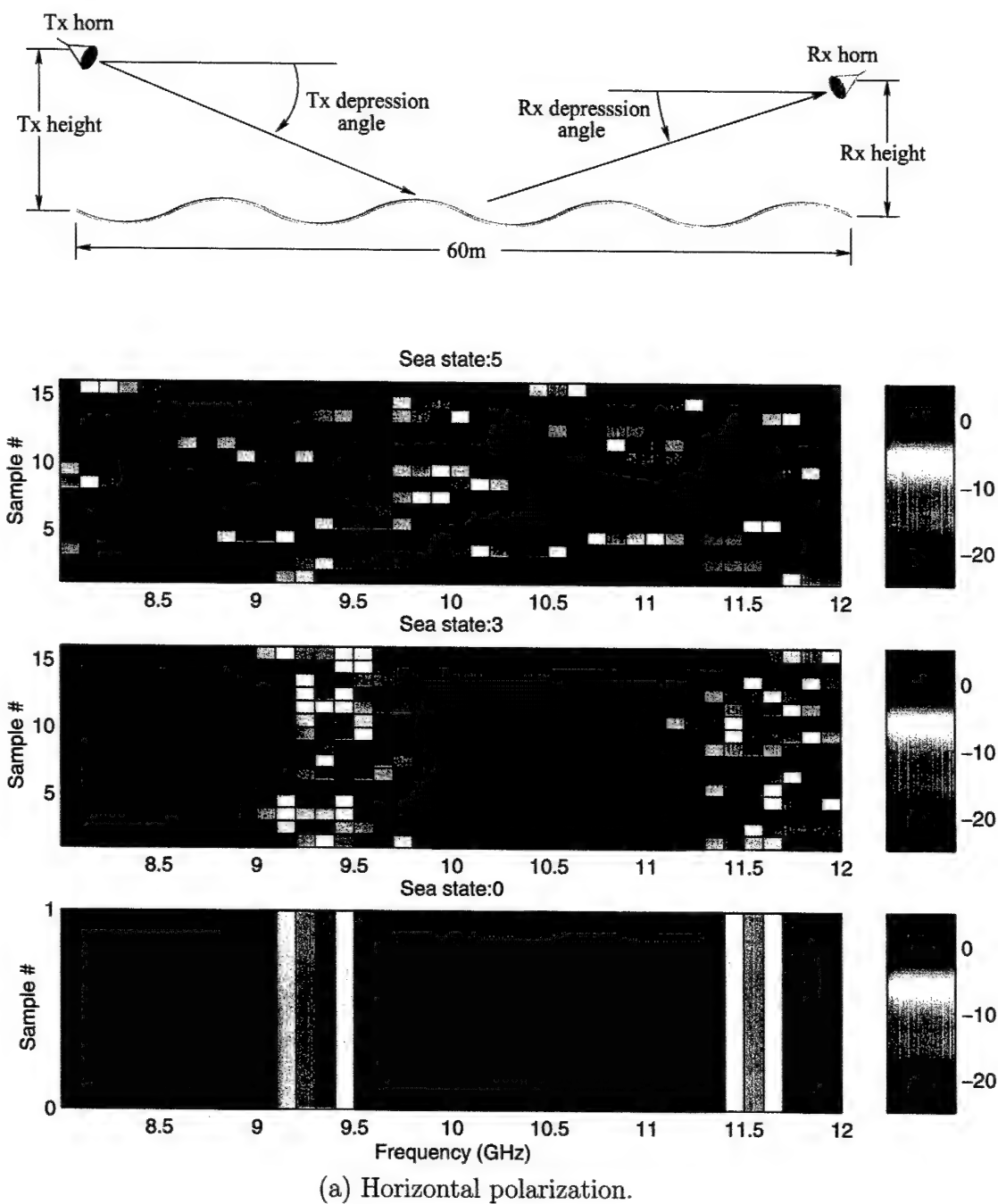
20

Figure 3.6: Contour plots of the forward scatter Monte Carlo data for sea states 3 and 5. Tx height = 5.25 m, Rx height = 1.75 m, Tx depression angle 9.9°. Color scales in dB.
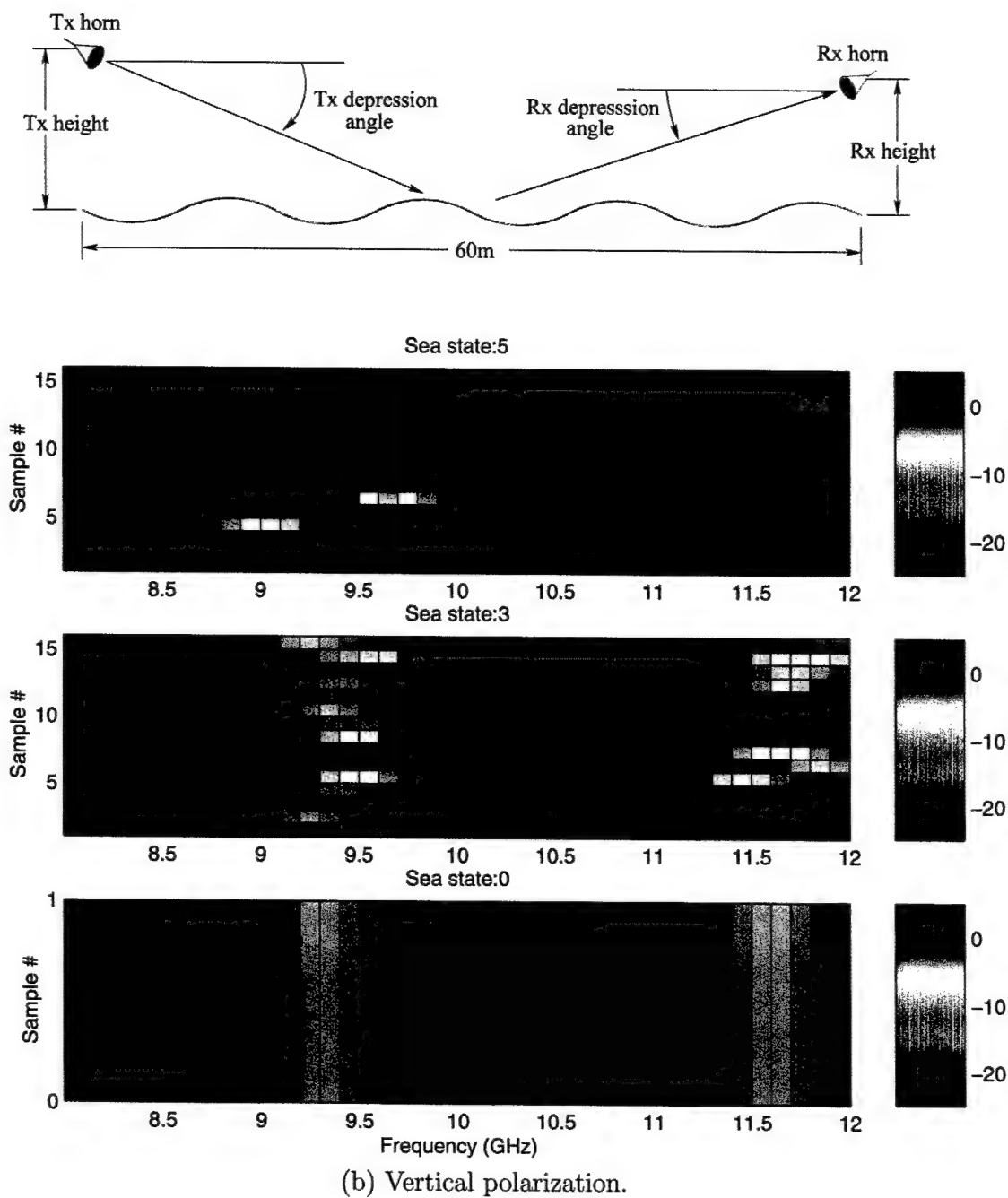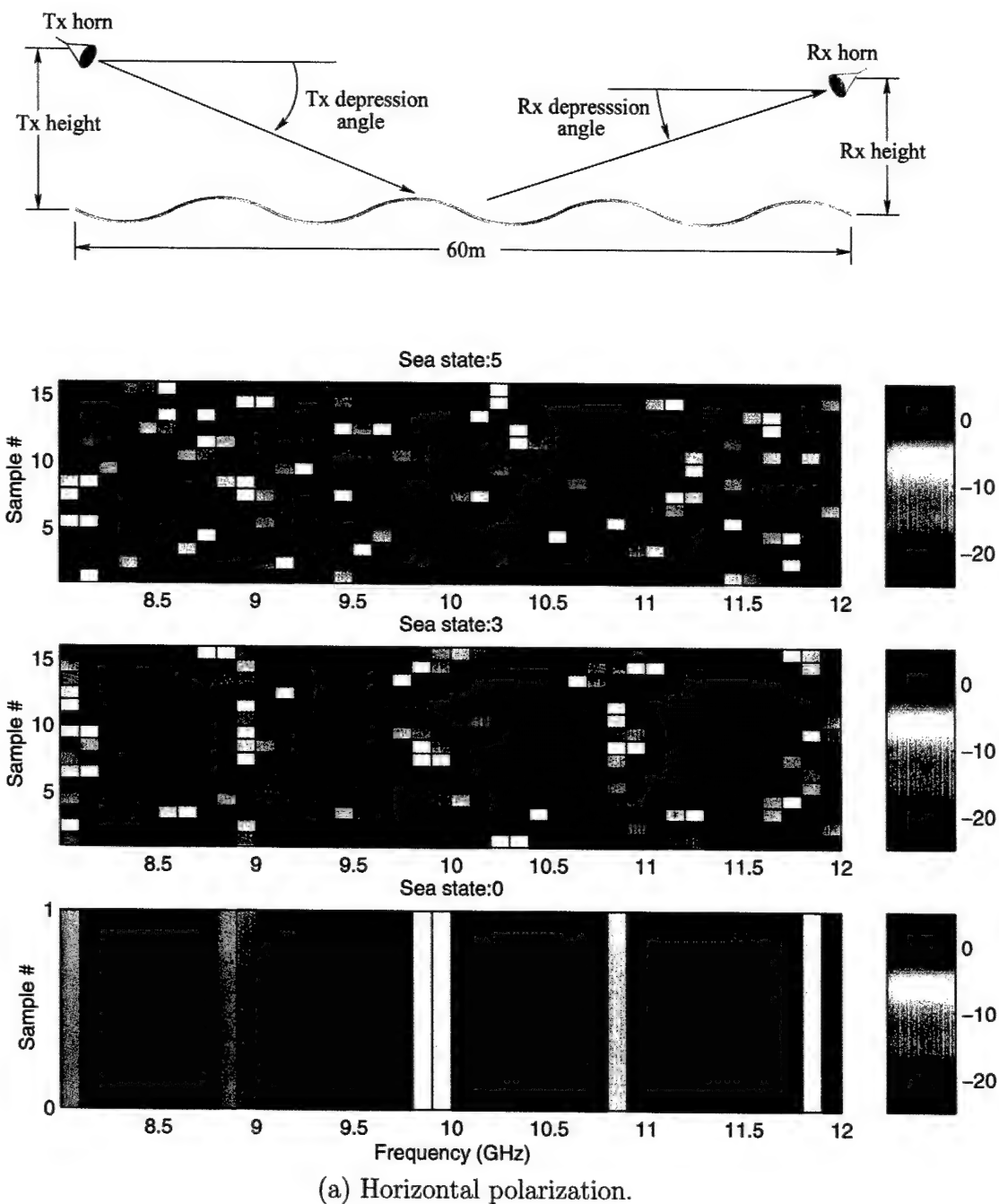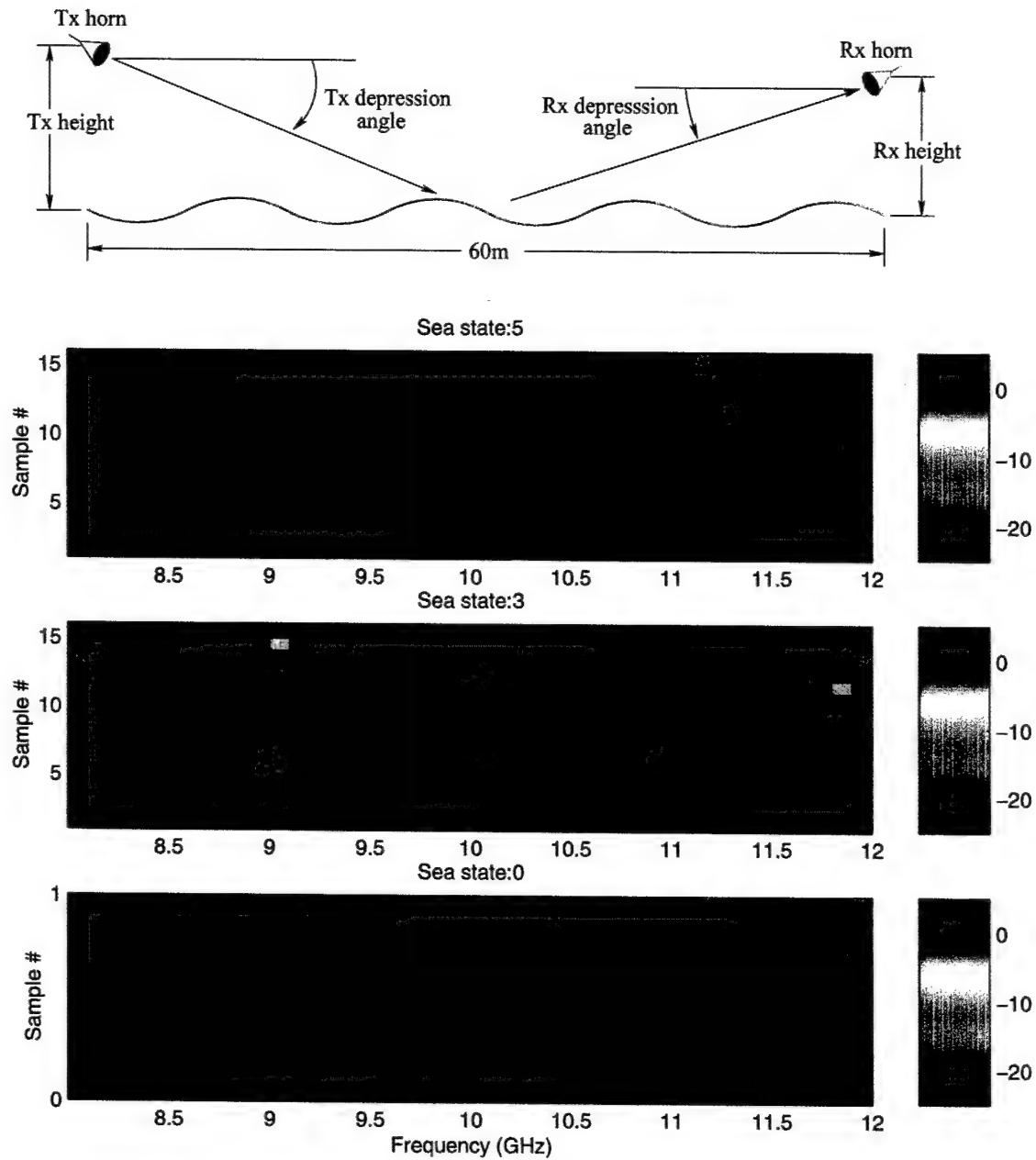
21

Figure 3.6: (cont'd.) Contour plots of the forward scatter Monte Carlo data for sea states 3 and 5. Tx height = 5.25 m, Rx height = 1.75 m, Tx depression angle 9.9°. Color scales in dB.

### 3.1.3  2D Forward Scatter Statistics

**Probability Density Function**

Figures 3.7 to 3.12 plot the probability density functions (PDFs) of the Monte Carlo data for the three horn positions for sea states 3 and 5. The mean gain is plotted in dB, which is $A = < |\tilde{E}|^2 >$ from (2.3) and (2.4), and the mean gain $\pm$ one standard deviation $\sigma$. Also included is the sea state 0 result (flat surface). The PDF plots clearly show the relative spread in the Monte Carlo data around the mean.
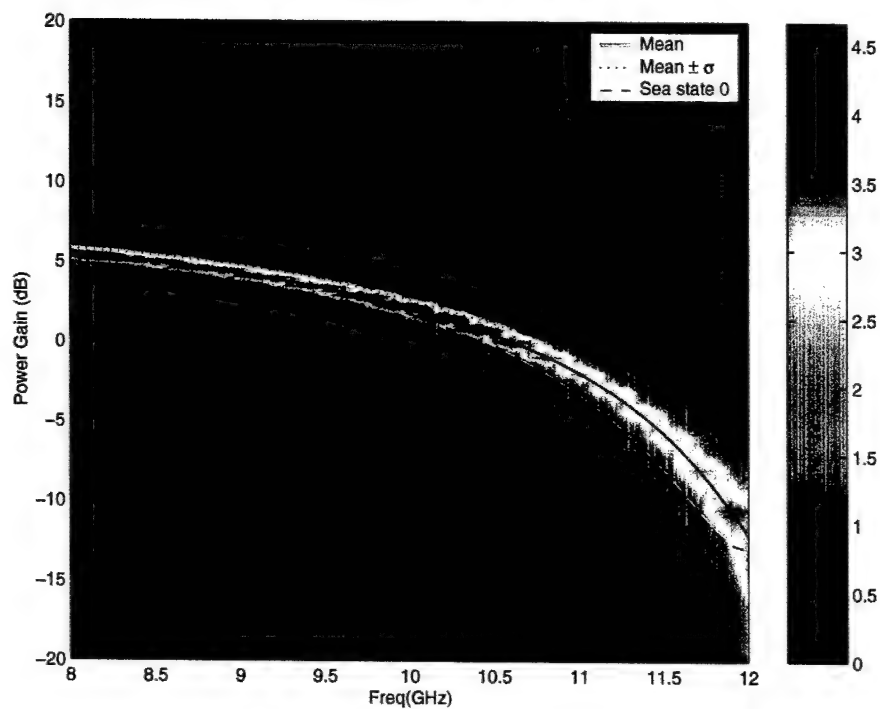
(a) Sea state 3.
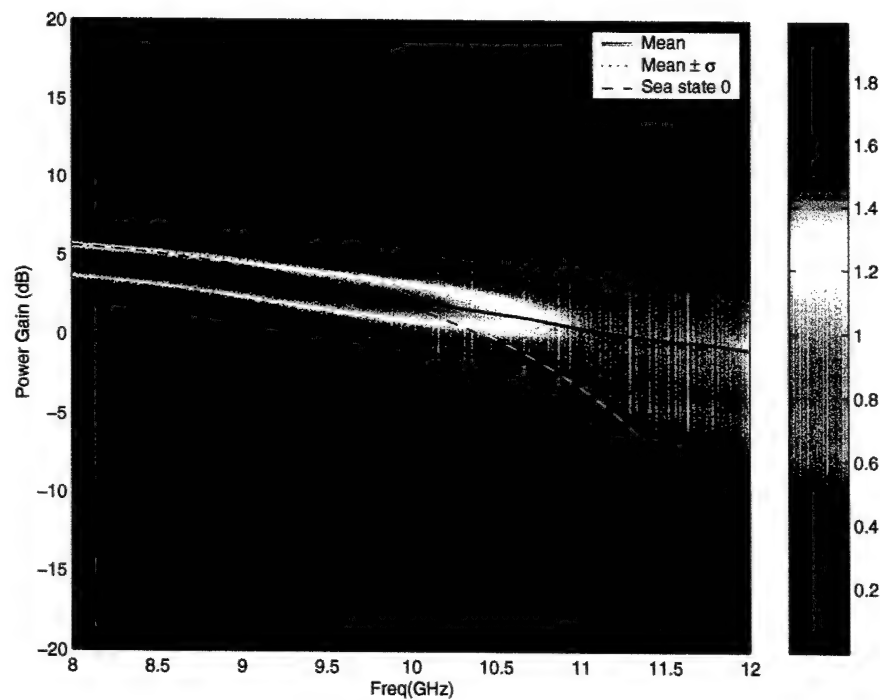


(b) Sea state 5.

Figure 3.7: Forward scatter probability density function for sea states 3 and 5, horizontal polarization. Tx height = 1.05 m, Rx height = 0.75 m, Tx depression angle 2°.

(a) Sea state 3.



(b) Sea state 5.

Figure 3.8: Forward scatter probability density function for sea states 3 and 5, vertical polarization. Tx height = 1.05 m, Rx height = 0.75 m, Tx depression angle 2°.

(a) Sea state 3.



(b) Sea state 5.

Figure 3.9: Forward scatter probability density function for sea states 3 and 5, horizontal polarization. Tx height = 3.14 m, Rx height = 1.25 m, Tx depression angle 6°.
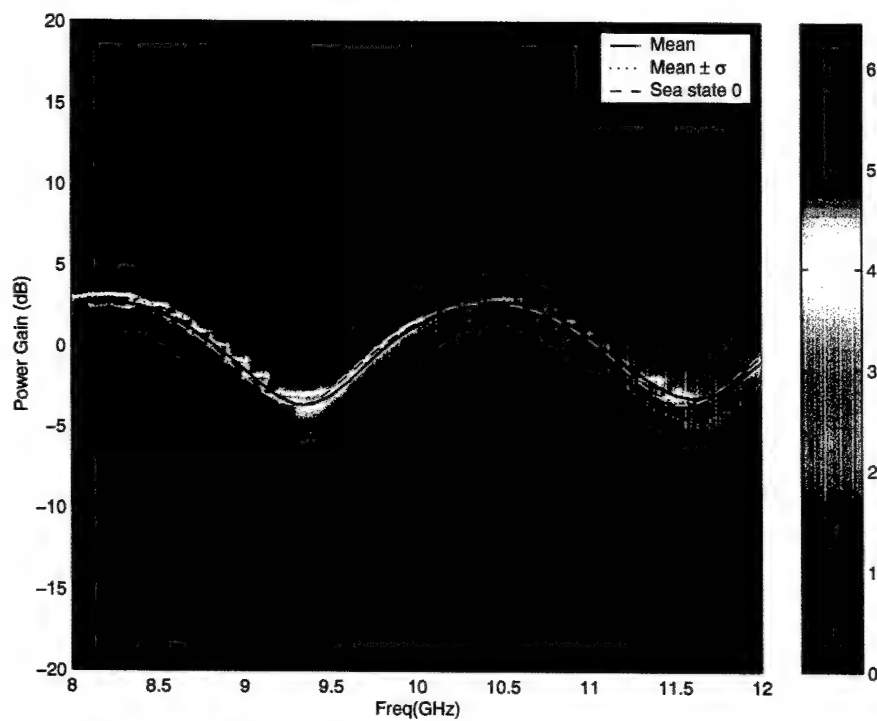
(a) Sea state 3.
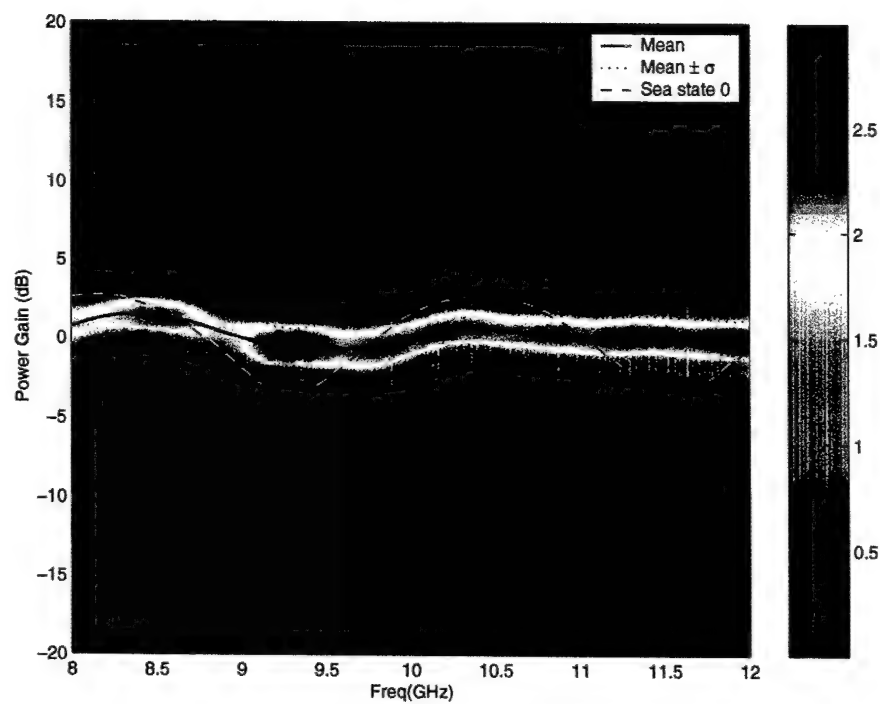


(b) Sea state 5.

Figure 3.10: Forward scatter probability density function for sea states 3 and 5, vertical polarization. Tx height = 3.14 m, Rx height = 1.25 m, Tx depression angle 6°.
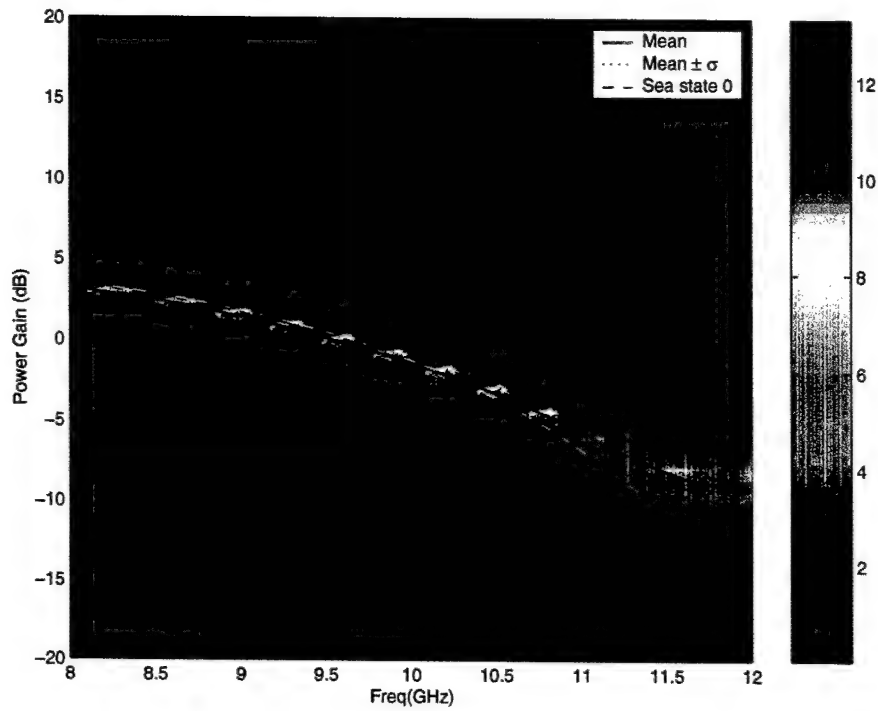
27

(a) Sea state 3.



(b) Sea state 5.

Figure 3.11: Forward scatter probability density function for sea states 3 and 5, horizontal polarization. Tx height = 5.25 m, Rx height = 1.75 m, Tx depression angle 9.9°.

(a) Sea state 3.


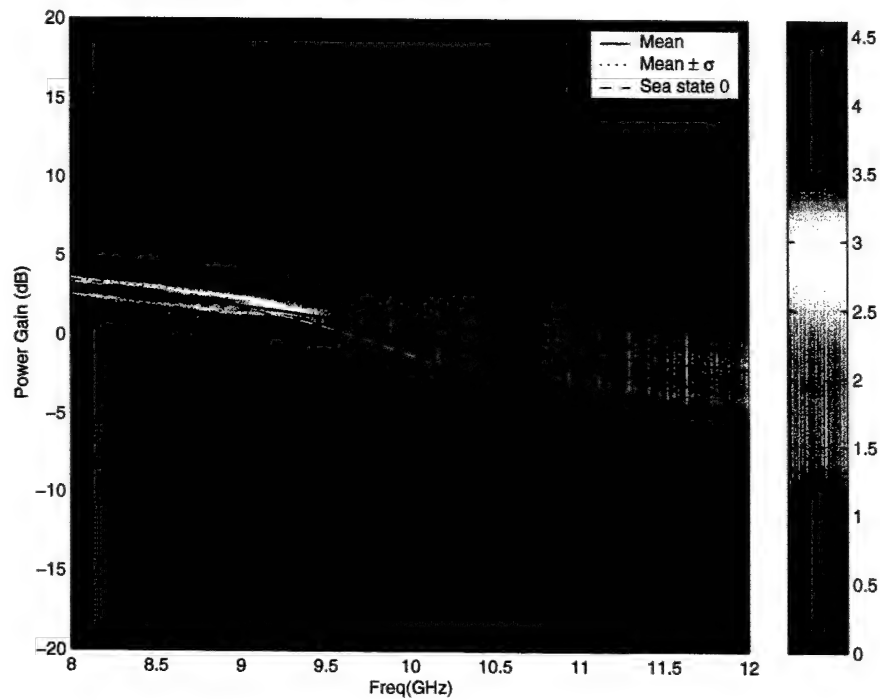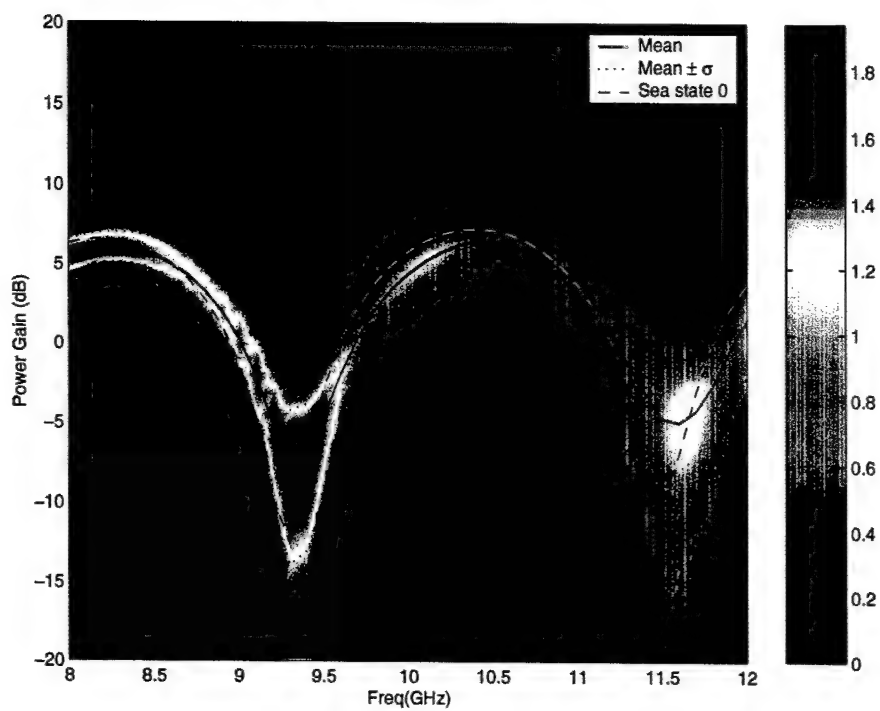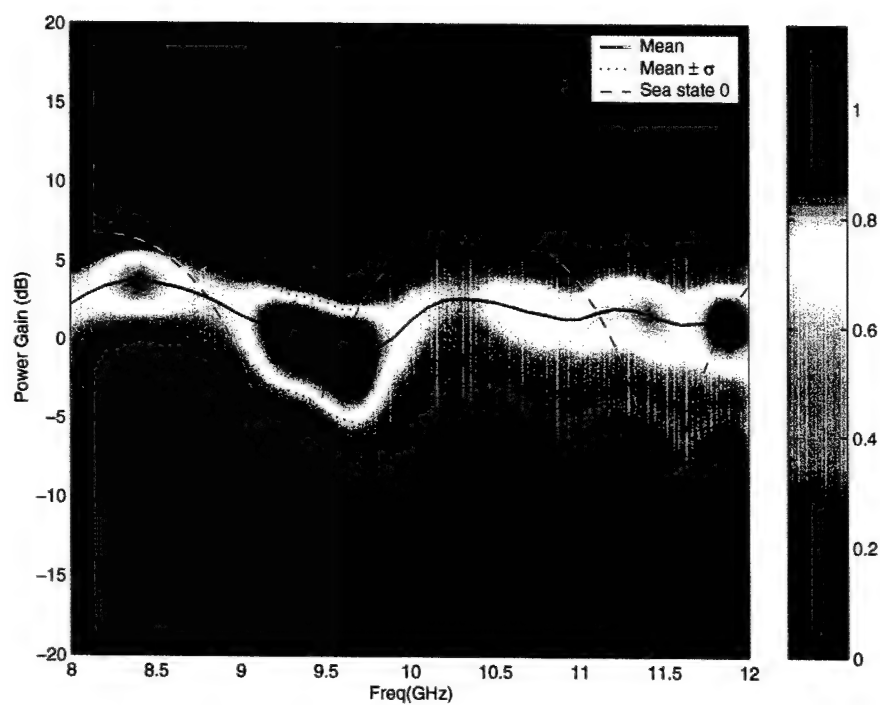
(b) Sea state 5.

Figure 3.12: Forward scatter probability density function for sea states 3 and 5, vertical polarization. Tx height = 5.25 m, Rx height = 1.75 m, Tx depression angle 9.9°.
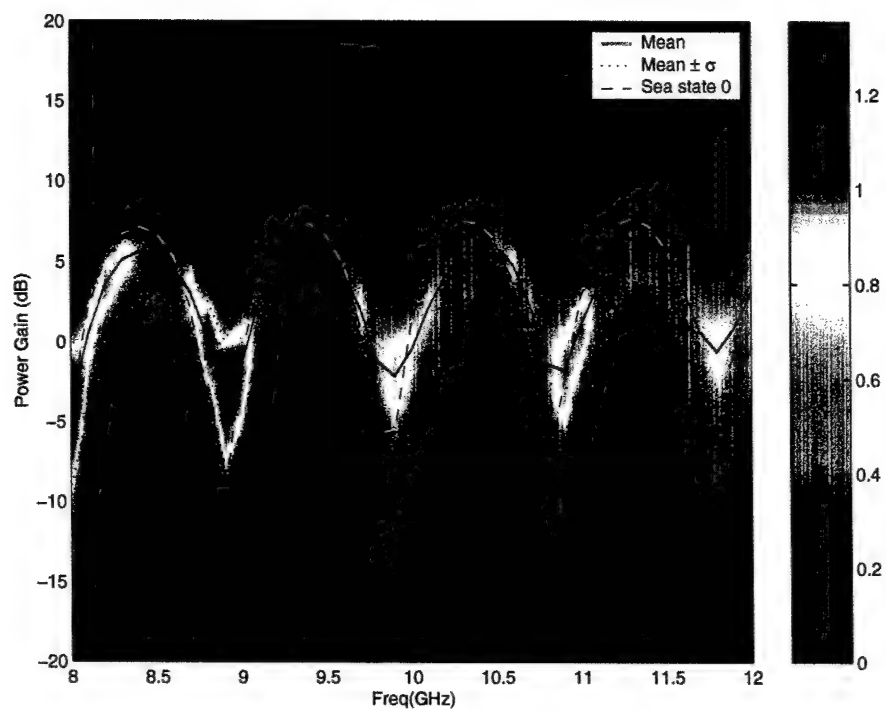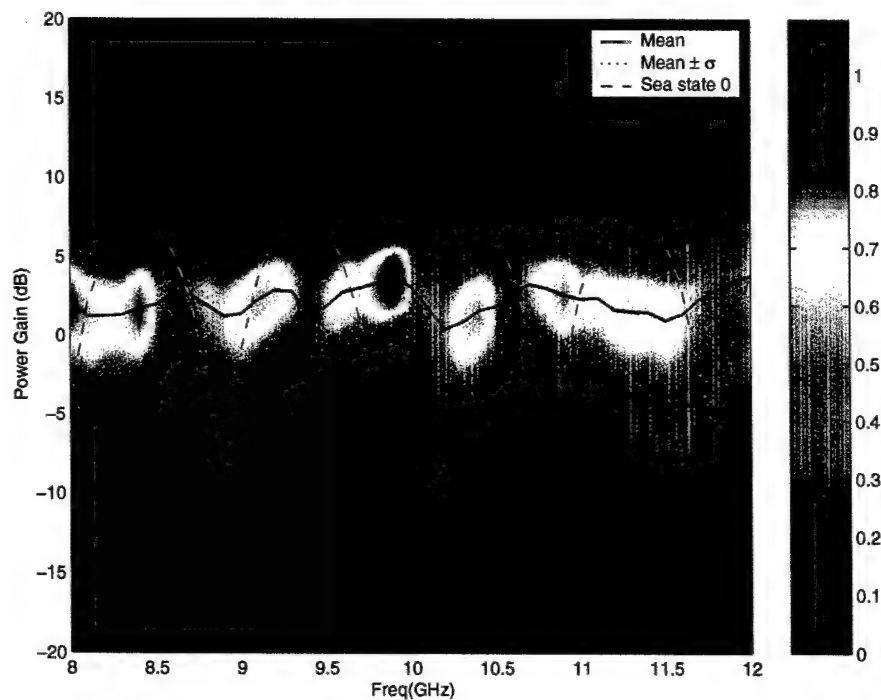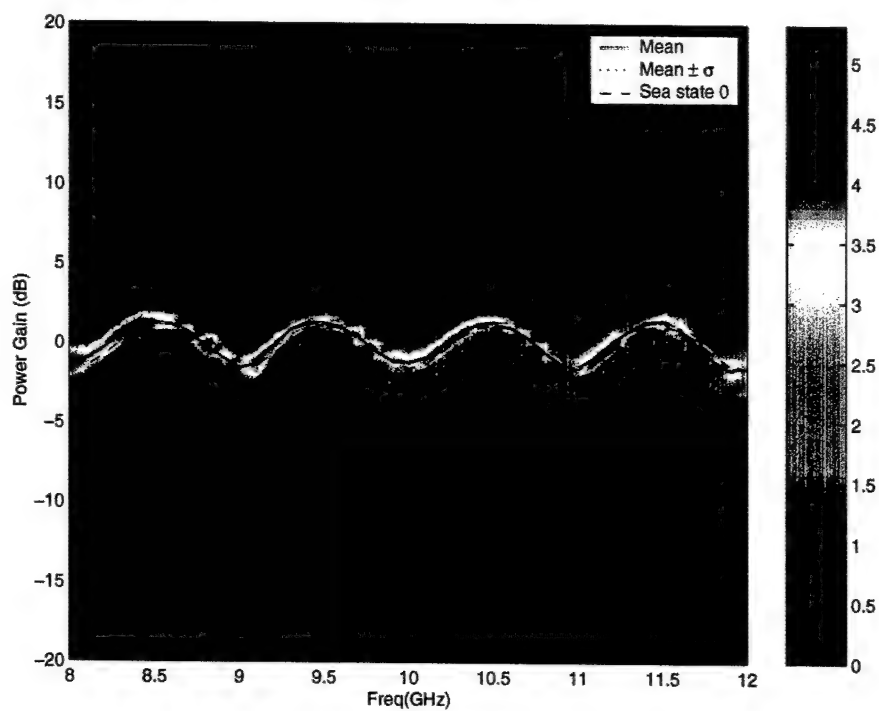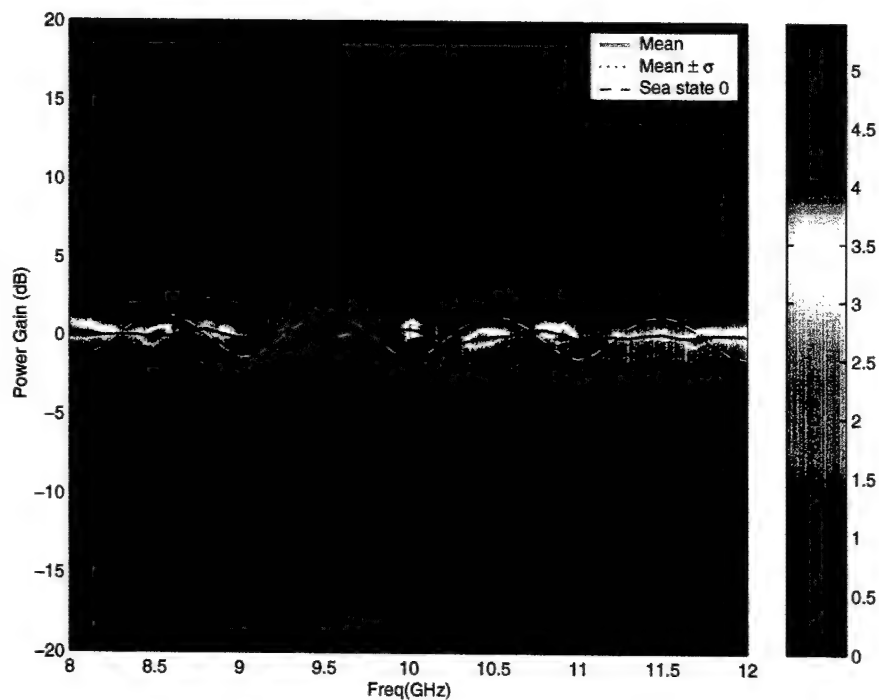
## Coherent and Incoherent Power

Figure 3.13 plots the coherent and incoherent forward scatter statistics for the lowest transmit and receive horn positions. Recall that the sum of the coherent and incoherent power is the mean gain $< |\tilde{E}|^2 >$ from (2.3). The flat surface case is also plotted for comparison. For this low grazing angle, the forward scattering is highly coherent for sea state 3, while the incoherent scattering becomes significant for sea state 5.

Figure 3.14 plots the coherent and incoherent forward scatter statistics for the middle transmit and receive horn positions. The forward scatter is again fairly coherent for sea state 3, and the coherent field approximately follows the interference pattern of the flat surface case. The sea state 5 results show the sea surface scattering has essentially been removed from the coherent normalized received field, which is around 0 dB. This is due to the randomness of the sea scattered field which is averaged out of the coherent result.

Figure 3.15 plots the coherent and incoherent forward scatter statistics for the highest transmit and receive horn positions. The sea state 3 results are again fairly coherent, while the sea state 5 results are close to 0 dB, which suggests that the sea scattering is averaged out. However, the incoherent field for H-pol is also close to 0 dB, which says that the incoherent sea scattering is nearly the equal in magnitude to the incident field. The incoherent V-pol results are similar, but reduced in magnitude by the surface reflection coefficient.
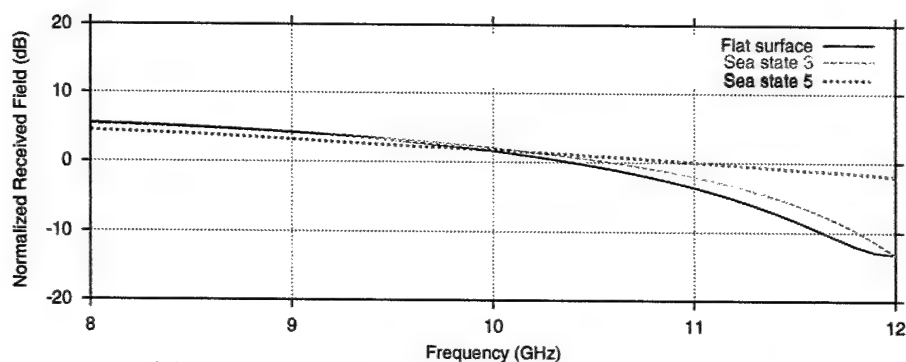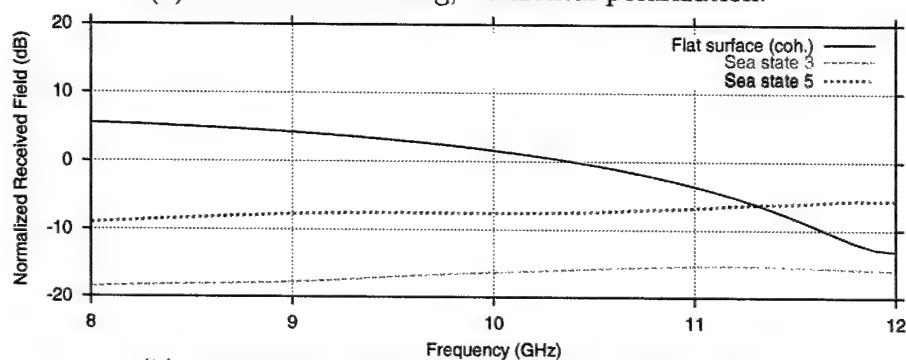
30

(a) Coherent scattering, horizontal polarization.



(b) Incoherent scattering, horizontal polarization.
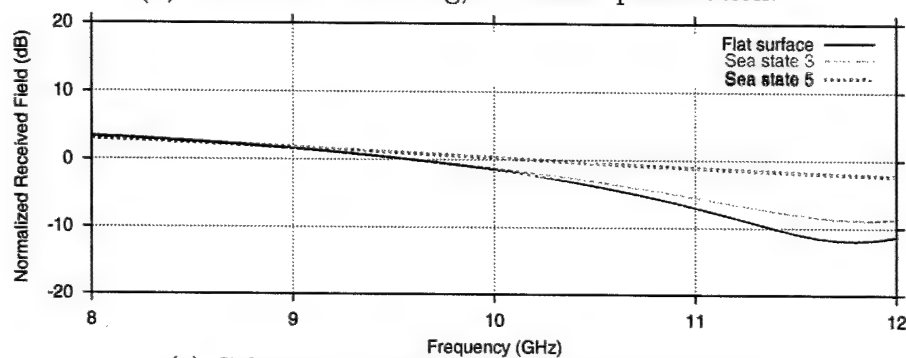


(c) Coherent scattering, vertical polarization.
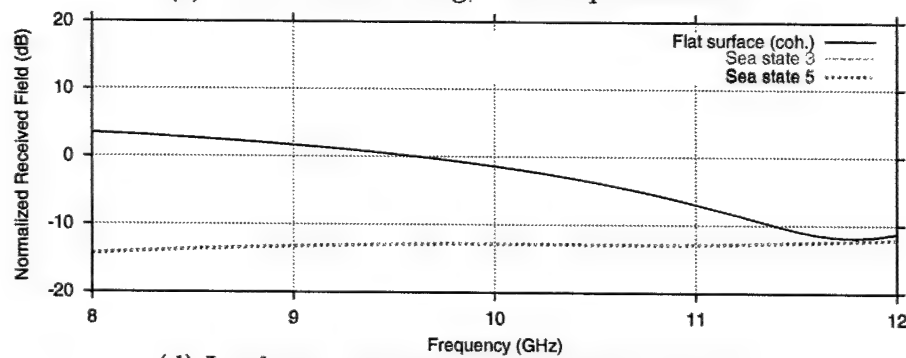


(d) Incoherent scattering, vertical polarization.

Figure 3.13: Coherent and incoherent forward scattering for sea states 3 and 5. Tx height = 1.05 m, Rx height = 0.75 m, Tx depression angle 2°.

31
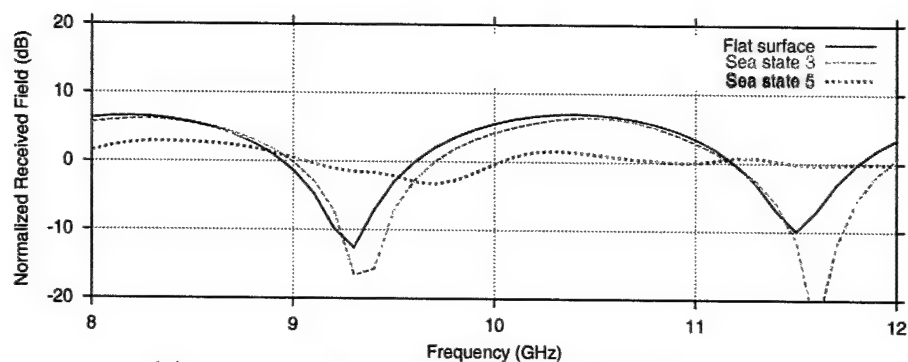
(a) Coherent scattering, horizontal polarization.
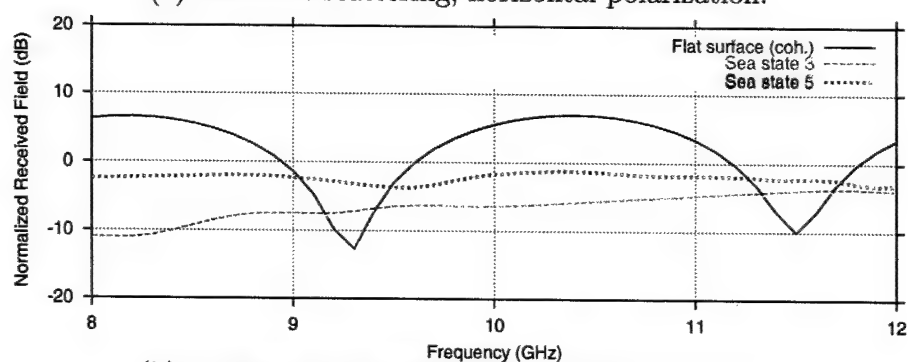


(b) Incoherent scattering, horizontal polarization.
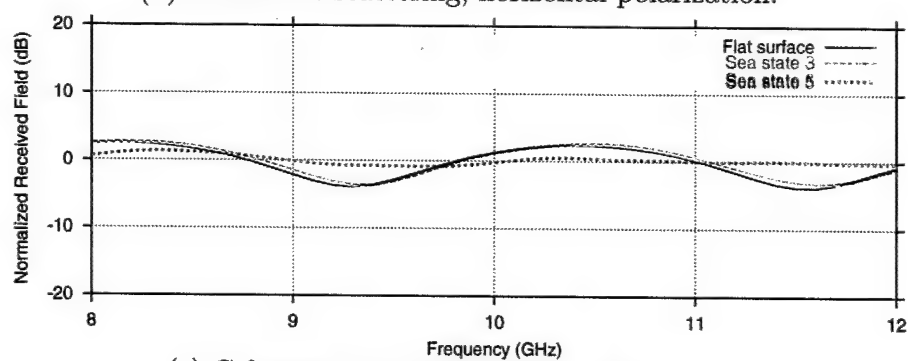


(c) Coherent scattering, vertical polarization.
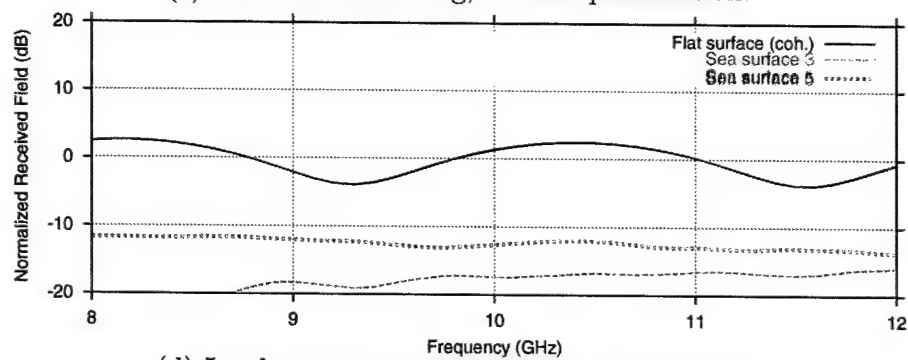


(d) Incoherent scattering, vertical polarization.

Figure 3.14: Coherent and incoherent forward scattering for sea states 3 and 5. Tx height = 3.14 m, Rx height = 1.25 m, Tx depression angle 6°.

32
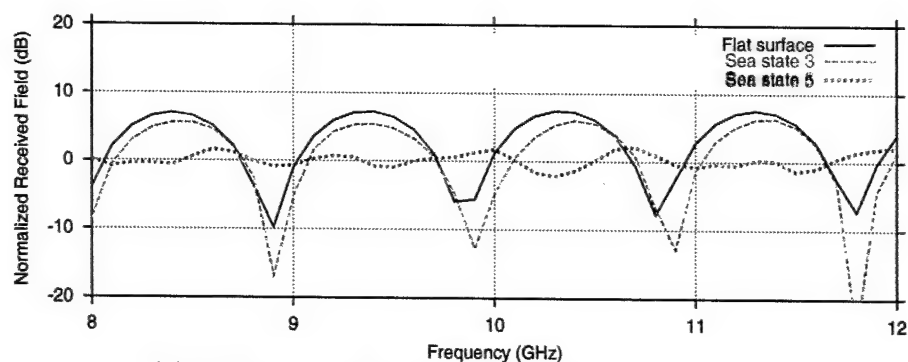
(a) Coherent scattering, horizontal polarization.
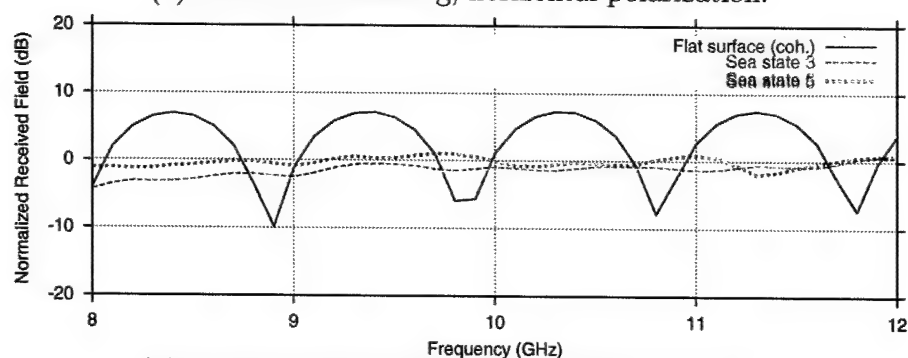


(b) Incoherent scattering, horizontal polarization.
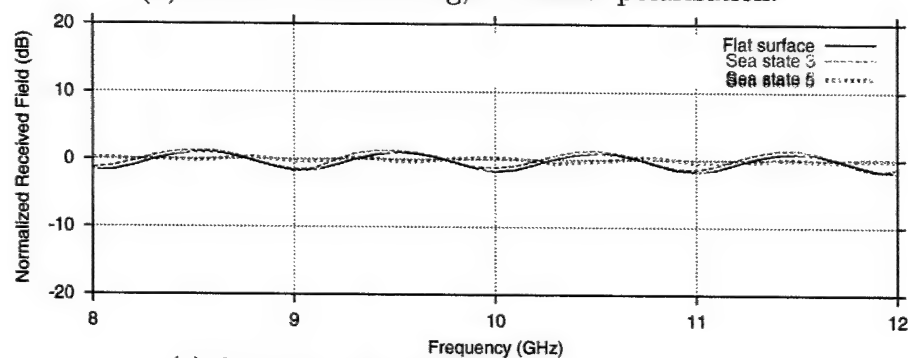


(c) Coherent scattering, vertical polarization.
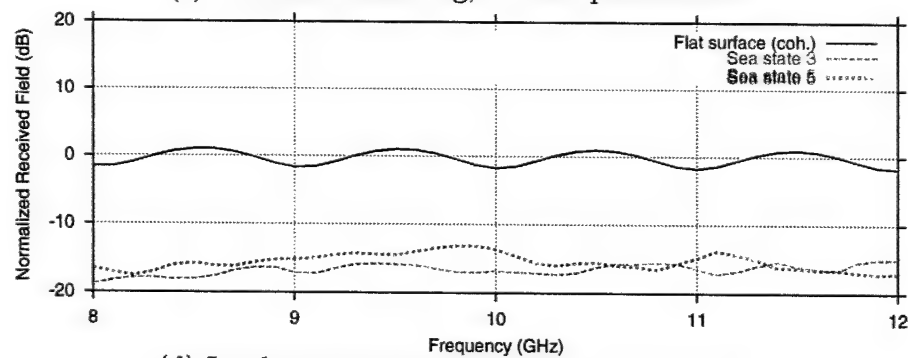


(d) Incoherent scattering, vertical polarization.

Figure 3.15: Coherent and incoherent forward scattering for sea states 3 and 5. Tx height = 5.25 m, Rx height = 1.75 m, Tx depression angle 9.9°.

33

## 3.2  3D Model using the Physical Optics Method

The area of the sea surface illuminated by the incident beam is about 2000x350 wavelengths at X-band, which translates to about 2.8 million physical optics (PO) sampling points. This is reasonable for a first order approximation, but is currently intractable for iterative physical optics (IPO). Therefore, only first order PO is used here to compute the forward scattering, as described in Section 1.2.1. This approximation neglects the surface-to-surface interactions. In this section some selected numerical results will be shown for accuracy comparisons, but a full Monte Carlo simulation will not be repeated.

Figures 3.16 and 3.17 show the normalized forward scattered fields for the highest transmit and receive horn positions, horizontal and vertical polarization, respectively. The 3D PO results are compared with the 2D GFB results for the same cases. The flat surface results of Figures 3.16(a) and 3.17(a) include the analytic reference solution. The sea state 3 and 5 results use a single realization of the Pierson-Moskowitz random sea surface.

The agreement between all the solutions is very good for the flat surface cases. However, the agreement between the GFB and PO solutions is only fair for sea state 3, and not very good for sea state 5. It is highly probable that the GFB solution is more accurate for these cases, even though it is a 2D solution. This is because the GFB method includes the surface-to-surface interactions between the waves, while first order PO does not. Furthermore, the crests of the ocean waves cast shadows on the surface which are not properly accounted for in the PO algorithm used here. The iterative PO solution would be able to correct for shadow boundaries and include surface-surface interactions, but would have to be validated with a smaller physical geometry.
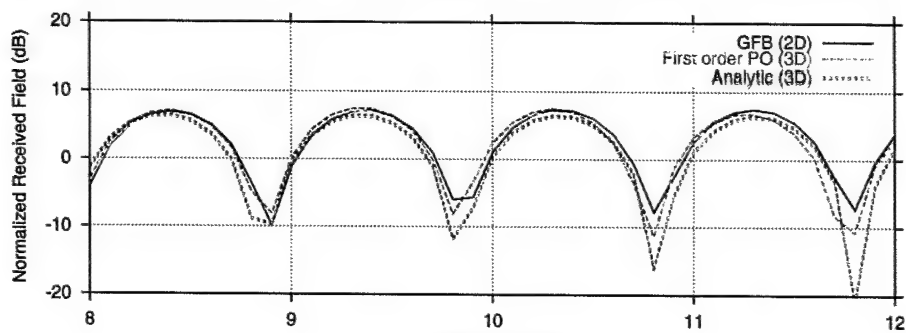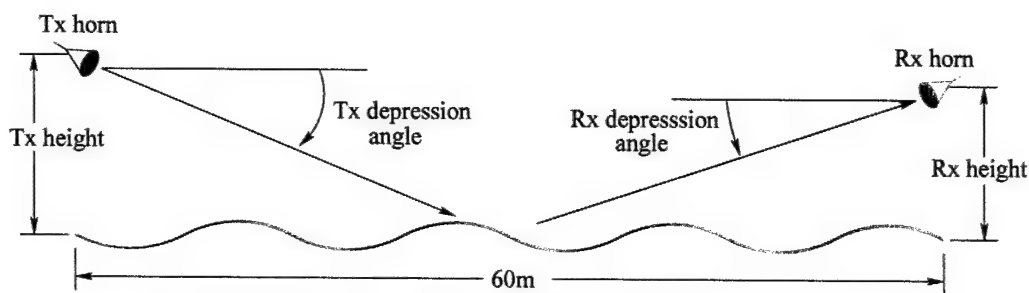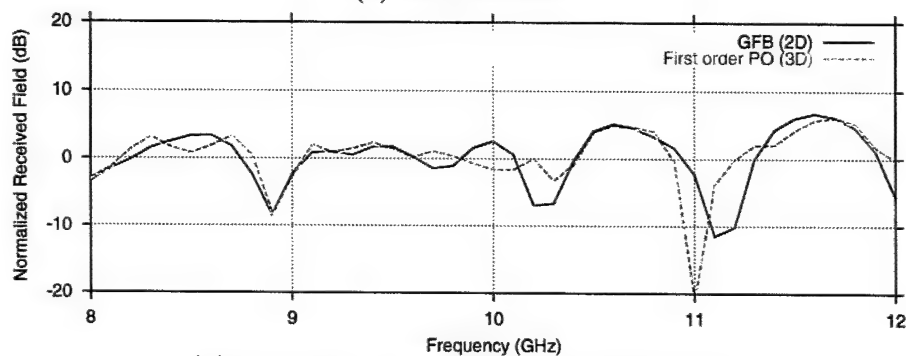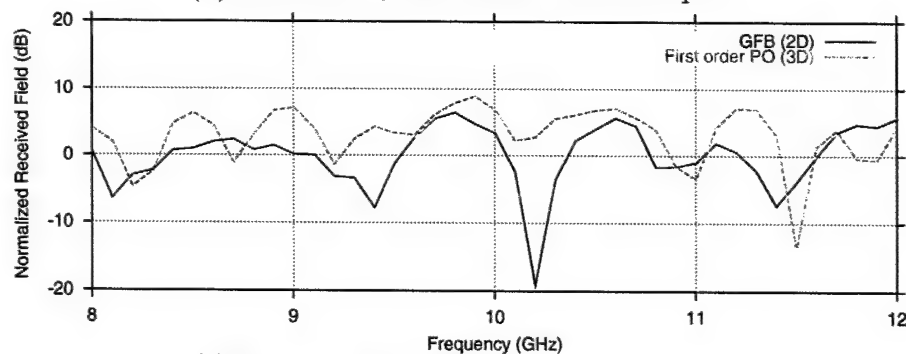
Figure 3.16: PO and GFB comparisons of forward scattering, horizontal polarization. Tx height = 5.25 m, Rx height = 1.75 m, Tx depression angle 9.9°.

35

(a) Flat surface.

(b) Sea state 3, first Monte Carlo sample.

(c) Sea state 5, first Monte Carlo sample.
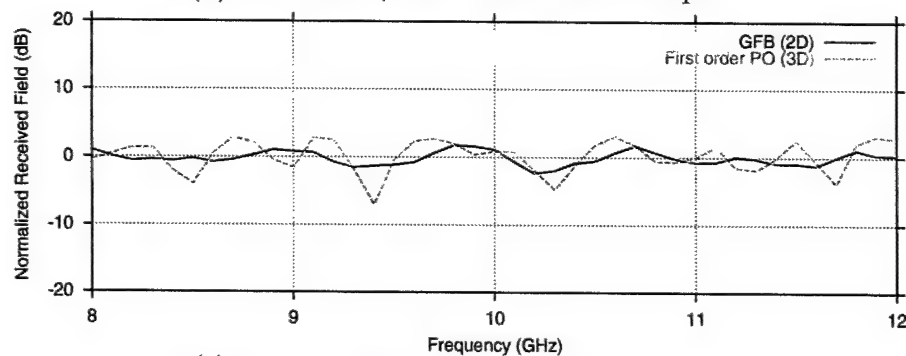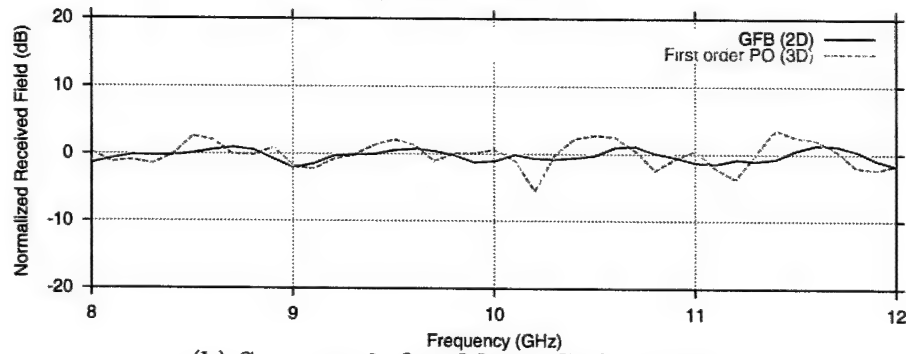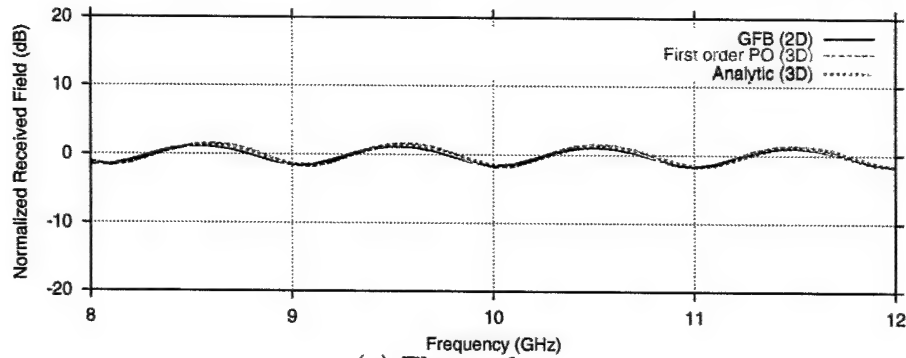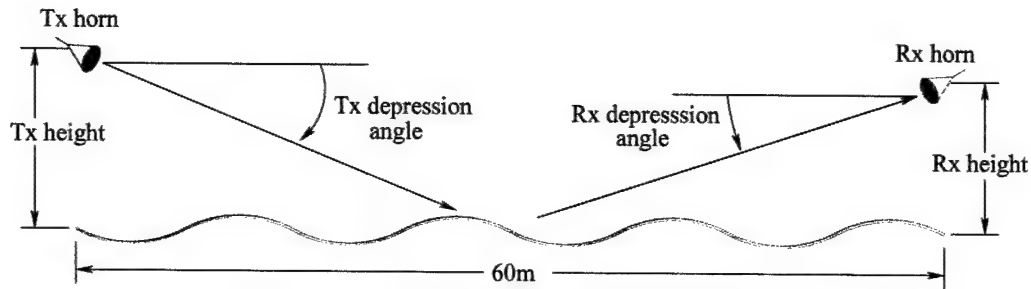
Figure 3.17: PO and GFB comparisons of forward scattering, vertical polarization. Tx height = 5.25 m, Rx height = 1.75 m, Tx depression angle 9.9°.

36

# Chapter 4

# Backscatter Simulations

The backscatter experimental set-up is shown again here in Figure 4.1. The backscatter from targets over the sea surface is computed in this chapter in the form of radar cross section (RCS), defined by

$$\text{RCS} = 4\pi R \frac{|E^s|^2}{|E^i|^2} \tag{4.1}$$

where $R$ is the range from the Tx/Rx horn to the target [15]. $E^i$ and $E^s$ are defined differently here than in Chapter 3. $|E^i|$ is the amplitude of the free space incident field in the target zone along the boresight (main beam) direction. $E^s$ is the total backscattered field received by the Rx horn. This simulates the experimental RCS which is calibrated by pointing the Tx/Rx horns directly at a perfect electrically conducting (PEC) sphere hanging sufficiently far above the sea surface.

The coherent and incoherent RCS are computed using the same formulas given in (2.3) with $\tilde{E}$ replaced by $E^s$, and scaled by a factor of $4\pi R/|E^i|^2$. In other words, the coherent
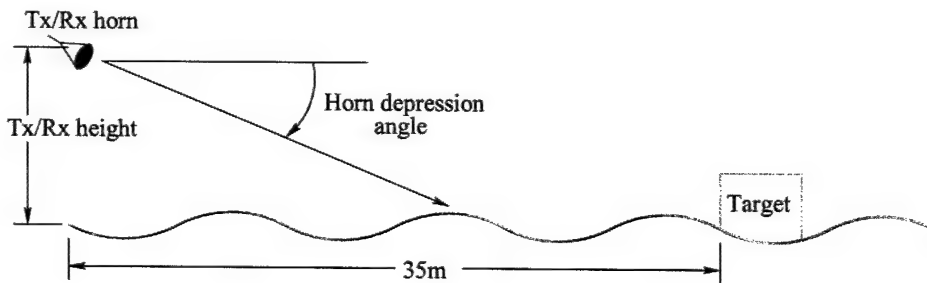


Figure 4.1: Experimental set-up for backscatter measurements over a rough sea surface.

37

and incoherent RCS is defined in terms of the complex backscattered electric field. The RCS units in the plots in decibels relative to a square meter (dBsm).

# 4.1 2D Model using the Generalized Forward Backward Method

The GFB method yields a 2D backscatter cross section that must be scaled in the third dimension to give a 3D RCS. For a target geometry that is translationally invariant in the third dimension and has width $W$ in this direction, the scale factor is simply $2W^2/\lambda$, where $\lambda$ is the free space wavelength. An example of such a target is a flat plate oriented transverse to the downrange direction. The backscatter results presented in this chapter are for a flat PEC plate that is 0.9144 m high and 0.2286 m wide. The center of the plate is 1.4224 m above the sea surface. Two orientations are considered: vertical and tilted away from the transmitter by 15°. This latter configuration is typical of low cross-section ship designs.

## 4.1.1 GFB Surface Clutter

Before presenting the backscatter data, it is important to evaluate the level of the surface clutter. Figure 4.2 plots the backscatter from single surface realizations with the target absent for sea states 3 and 5. The backscatter is given in the same units as with the target present, i.e., RCS in dBsm, and is normalized using the same 2D-to-3D scaling factor of $2W^2/\lambda$ where $W = 0.2286$ m. (Note that the surface clutter is not normalized to surface area.) Therefore, the surface clutter contribution in the simulations should be the same as in the measurements. It is possible that the scattering from the target is less than the average surface clutter level, in which case the measurements may not be able to discern the presence of the target without a coherent average. Note that the sea state 3 and 5 clutter is about the same level. This agrees with the two-scale model which states that the low grazing angle backscatter is dominated by Bragg scattering from the capillary waves, which are relatively independent of the wind speed (assuming no breaking waves are present) [15]. Also note the clutter for vertical polarization (V-pol) is about 10 dB higher than for H-pol, which is also

38

consistent with other clutter models.

*Please note that the clutter computed by GFB with the Pierson-Moskowitz sea surface model is probably not the same as the measurements.* This is because the capillary waves are excited to a large extent by the wind, and there was no wind present in the MASK wave tank. Furthermore, the hydrodynamics measurements shown in Figure 2.1 only go down to an ocean wavelength of about 30 cm, which is considerably larger than the wavelengths responsible for sea clutter (which are on the order of the electromagnetic wavelength). This is not to say that smaller scale waves are not present in the experiments, but that they were not measurable. The clutter plots shown in Figure 4.2 are used here only for evaluating the surface clutter contribution to the computed results. It will be seen that the backscatter from the tilted plate is lost in the surface clutter for V-pol, but the coherent averaging extracts the expected signature.
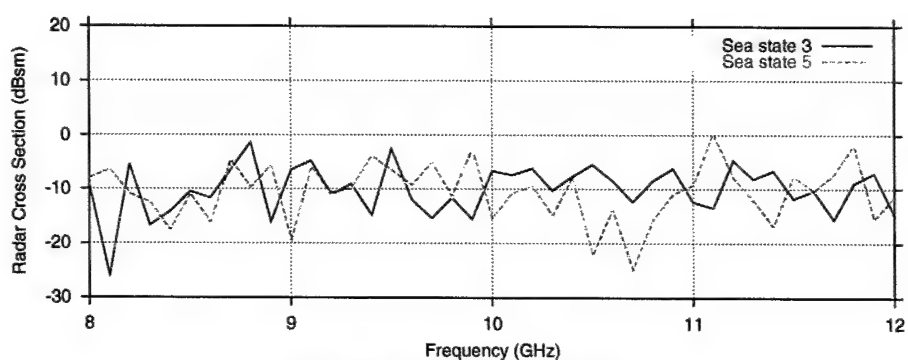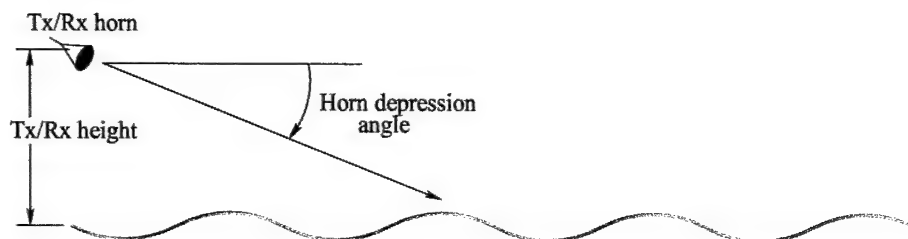
(a) Horizontal polarization.
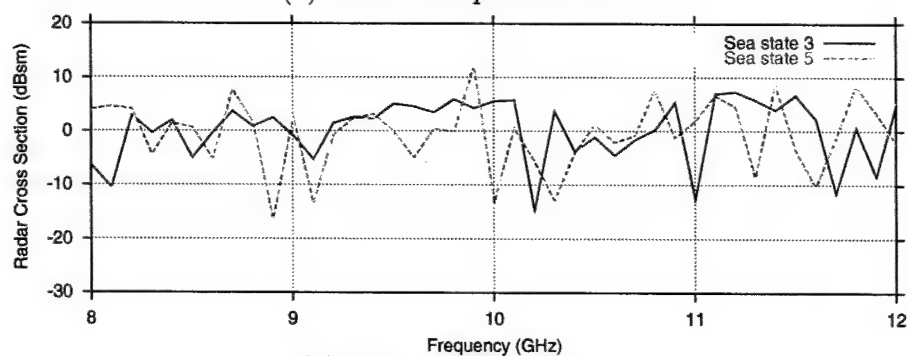


(b) Vertical polarization.

Figure 4.2: Surface clutter for single realizations of the sea surface for sea states 3 and 5. Tx/Rx height = 3.15 m, Horn depression angle = 9.9°.

40
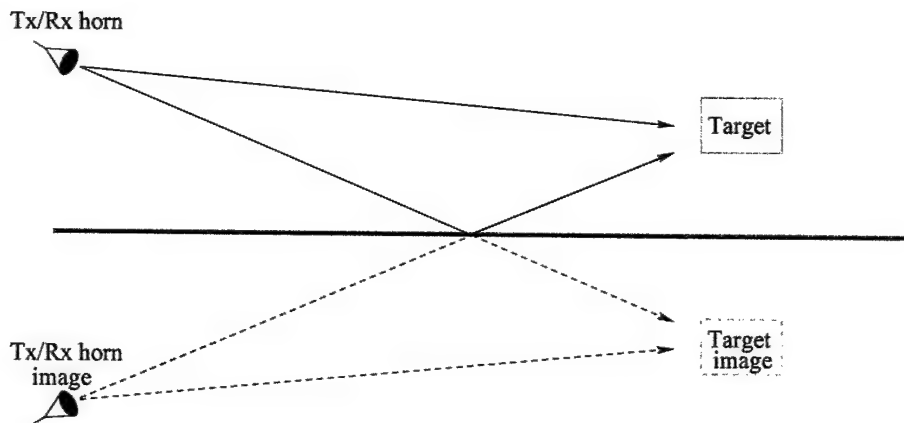
Figure 4.3: Image theory used to obtain the backscatter reference solution.

## 4.1.2  3D Backscatter Reference Solution

The backscatter numerical simulations for a flat sea surface are compared here with an analytic solution based on image theory. This solution is obtained by finding the incident and reflected (image) fields via geometrical optics as shown in Figure 4.3, and using first order PO. The sea-reflected field is modified by the appropriate plane wave reflection coefficient for sea water given in (3.2). Reciprocity is used to compute the backscattered field by reacting the incident field with the PO currents on the target as described in [1]. PO is expected to give good accuracy for the electrically large and geometrically simple targets considered here.

Figures 4.4 and 4.5 shows the analytic comparisons with the GFB method for the vertical and tilted flat plate targets, respectively. (Note that the vertical RCS scale is shifted down by 10 dB for the tilted plate with respect to the vertical plate.) The agreement is very good. As expected, the tilted plate RCS is considerably lower than the vertical plate. The vertical plate is expected to have a high RCS because the vertical plate forms a partial corner reflector with the flat sea surface. Also note that for V-pol the tilted plate RCS is below the surface clutter level shown in Figure 4.2. Therefore it is expected that the Monte Carlo data will be dominated by surface clutter for this case, but the coherent RCS should be discernible from the clutter after processing.

41
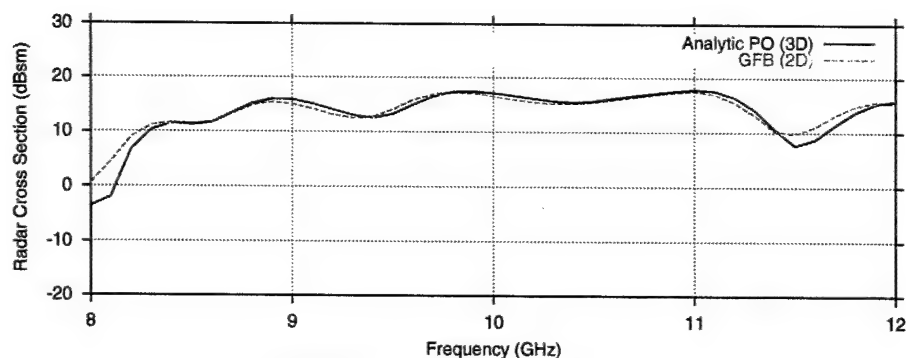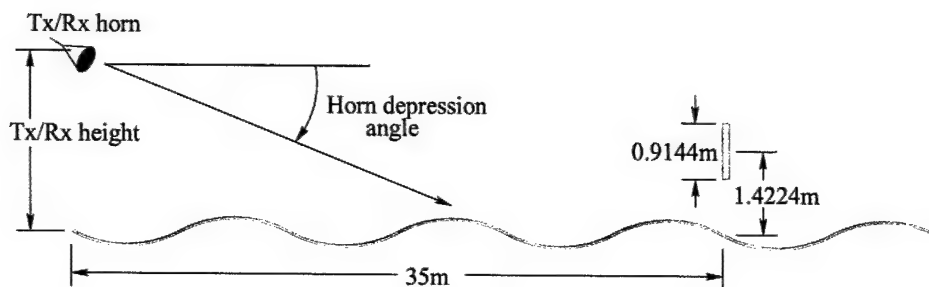
(a) Horizontal polarization.
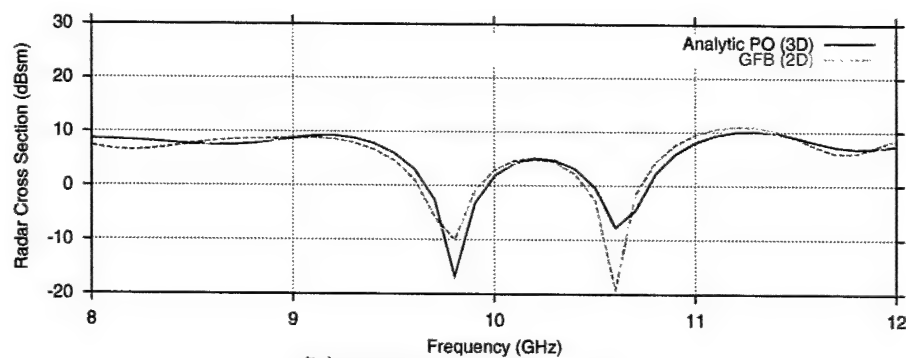


(b) Vertical polarization.

Figure 4.4: Analytic reference solution comparisons for backscatter from a vertical flat plate target over a flat sea surface. Tx/Rx height = 3.15 m, Horn depression angle = 9.9°.

(a) Horizontal polarization.
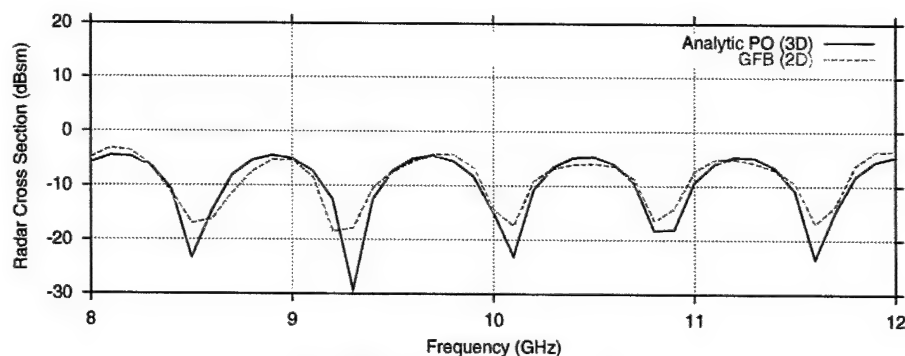


(b) Vertical polarization.

Figure 4.5: Analytic reference solution comparisons for backscatter from a tilted flat plate target over a flat sea surface. Tx/Rx height = 3.15 m, Horn depression angle = 9.9°.

43

### 4.1.3 GFB backscatter Data

Figure 4.6 shows color contour plots of the Monte Carlo RCS data for the vertically oriented flat plate target with the highest Tx/Rx position. Sea states 0 (flat surface), 3 and 5 are plotte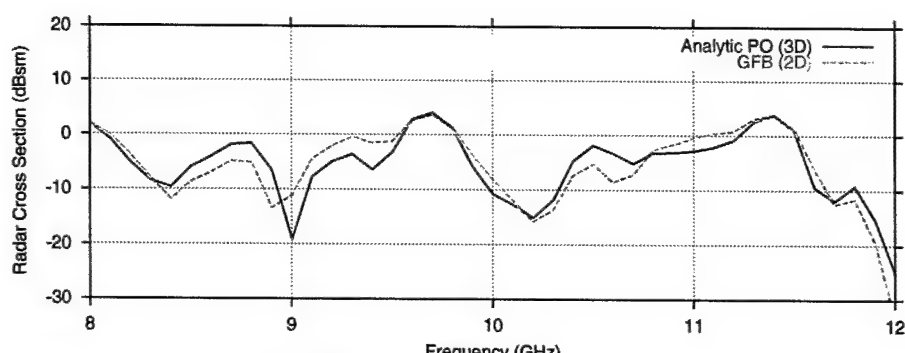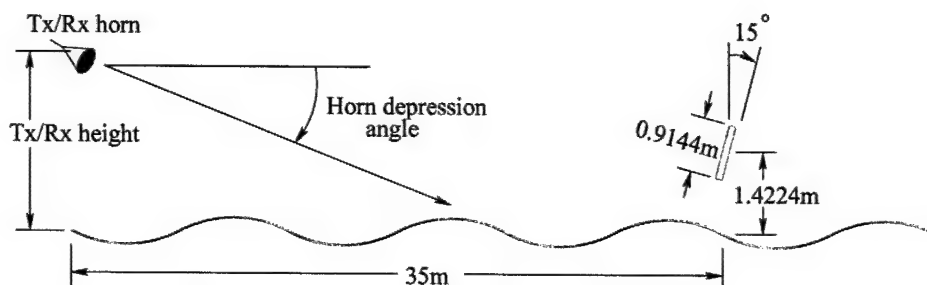d as a function of frequency from 8-12 GHz, for horizontal and vertical polarization. The color units for RCS are in dB relative a square meter (dBsm). This target is expected to have a high RCS because the vertical plate forms a partial corner reflector with the flat sea surface. The Monte Carlo data appears to be highly incoherent for both sea states 3 and 5. A significant portion of this incoherence may be due to the surface clutter, especially for V-pol. The H-pol results are significantly higher than V-pol due to the difference in the sea surface reflection coefficient, which indicates that the surface-target interactions are important.

Figure 4.7 shows color contour plots of the Monte Carlo RCS data for the tilted flat plate target with the highest Tx/Rx position. As expected, the RCS levels are much lower for this target compared with the vertically oriented plate. (Note that the color scale is shifted down by 10 dB with respect to the vertical plate results.) Again, the RCS appears to be highly incoherent for both sea states 3 and 5. It is interesting to note that the sea state 3 and 5 results for V-pol are significantly higher than the flat surface RCS (sea state 0), which is below the level of the surface clutter shown in Figure 4.2(b). This shows the backscatter is dominated by surface clutter.

44
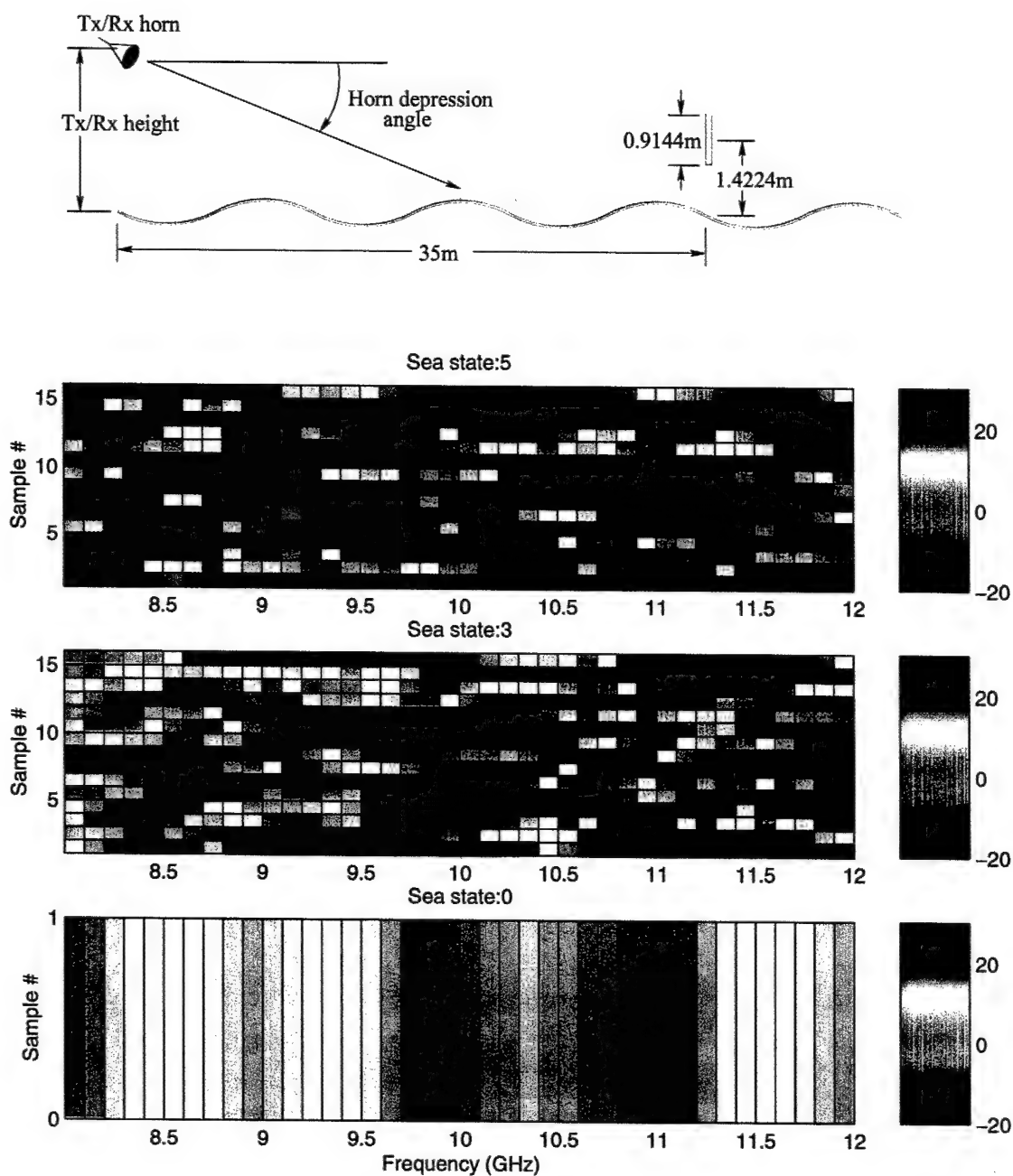
Figure 4.6: Contour plots of the backscatter Monte Carlo data for sea states 3 and 5. Target is a vertically oriented flat plate. Tx/Rx height = 3.15 m, Horn depression angle = 9.9°. Color scales in dBsm.
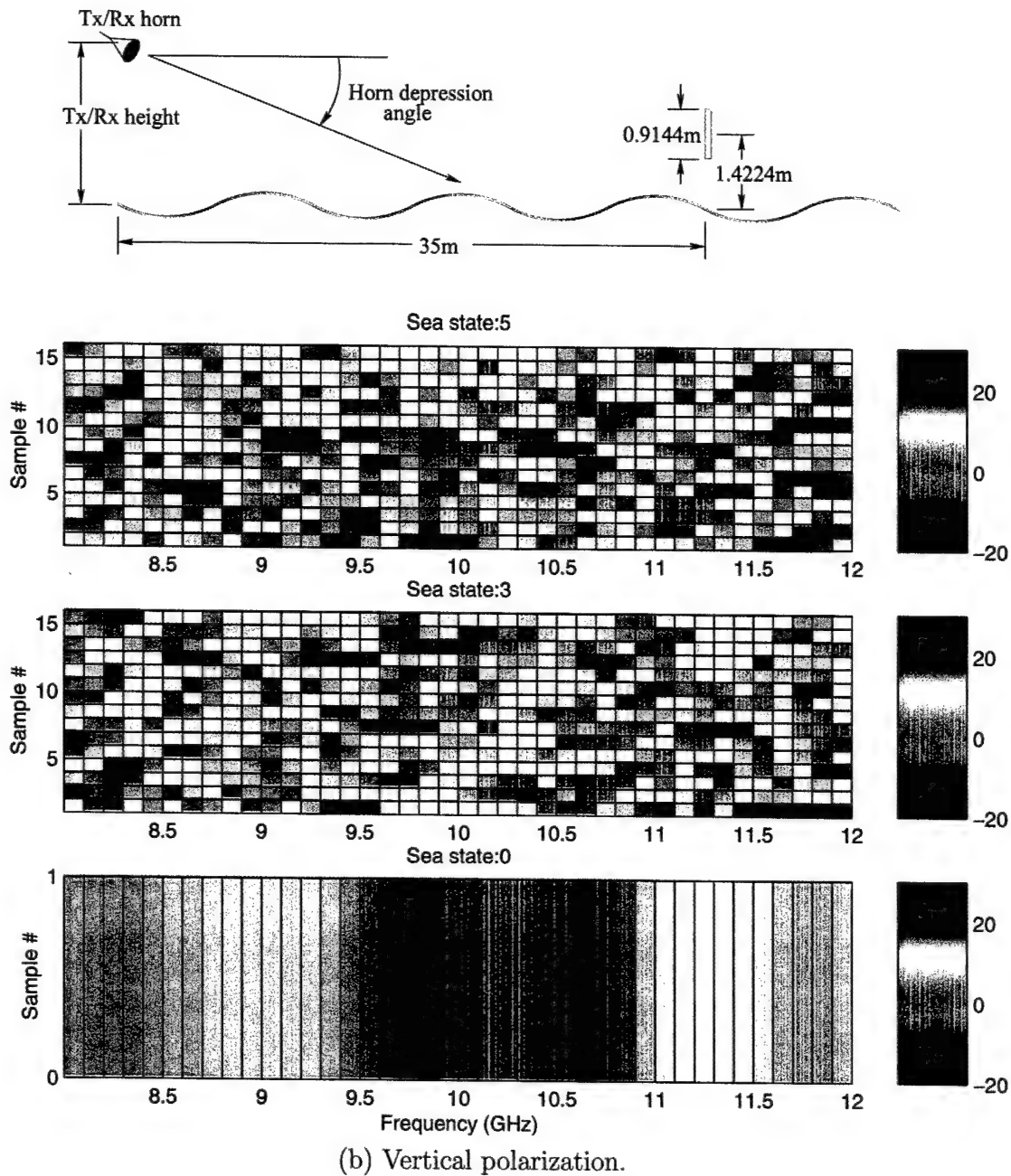
Figure 4.6: (cont'd.) Contour plots of the backscatter Monte Carlo data for sea states 3 and 5. Target is a vertically oriented flat plate. Tx/Rx height = 3.15 m, Horn depression angle = 9.9°. Color scales in dBsm.

46

(a) Horizontal polarization.

Figure 4.7: Contour plots of the backscatter Monte Carlo data for sea states 3 and 5. Target is a tilted flat plate. Tx/Rx height = 3.15 m, Horn depression angle = 9.9°. Color scales in dBsm.

47

Figure 4.7: (cont'd.) Contour plots of the backscatter Monte Carlo data for sea states 3 and 5. Target is a tilted flat plate. Tx/Rx height = 3.15 m, Horn depression angle = 9.9°. Color scales in dBsm.

48

## 4.1.4  GFB Backscatter Statistics

Figure 4.8 plots the coherent and incoherent scattering from the vertical plate target. The flat surface case is also included for comparison. The H-pol results are sufficiently high with respect to the surface clutter to assume that the target scattering dominates the return, while the V-pol levels are comparable to the clutter. The coherent RCS is comparable to the flat surface RCS, but the incoherent RCS tends to be somewhat higher.

Figure 4.9 plots the coherent and incoherent scattering from the tilted plate target. For H-pol the coherent RCS for sea states 3 and 5 is somewhat lower than the flat surface case, and the incoherent RCS is comparable. However, for V-pol the coherent scattering is significantly lower than the incoherent, which is clearly dominated by the surface clutter. Another important feature of the vertical polarization case is that the coherent scattering for sea states 3 and 5 is somewhat higher than the flat surface RCS. Therefore, the rough sea surface appears to enhance the RCS of the tilted plate.
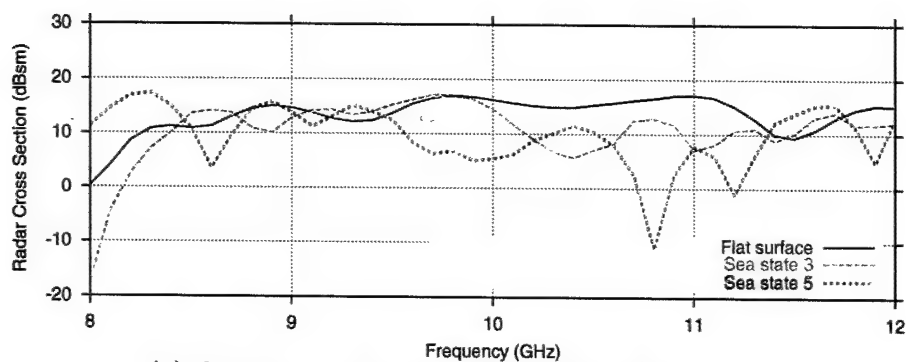
(a) Coherent scattering, horizontal polarization.
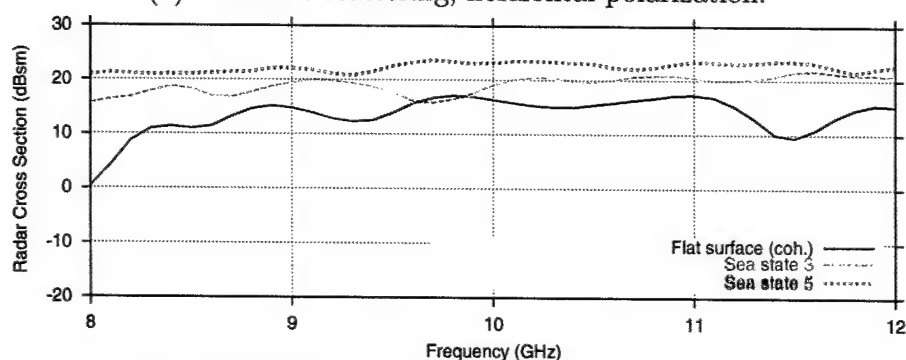


(b) Incoherent scattering, horizontal polarization.
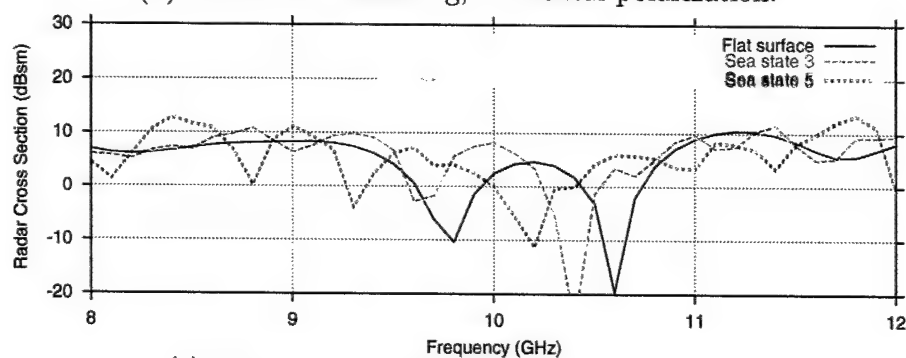


(c) Coherent scattering, vertical polarization.
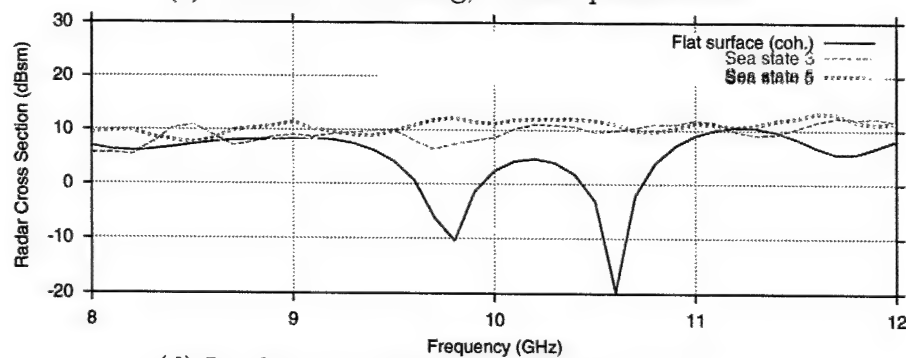


(d) Incoherent scattering, vertical polarization.

Figure 4.8: Coherent and incoherent backscattering for sea states 3 and 5. Target is a vertically oriented flat plate. Tx/Rx height = 3.15 m, Horn depression angle = 9.9°.

50
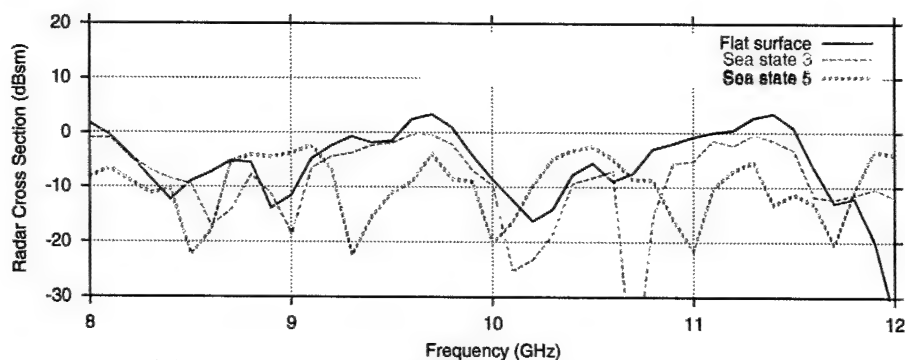
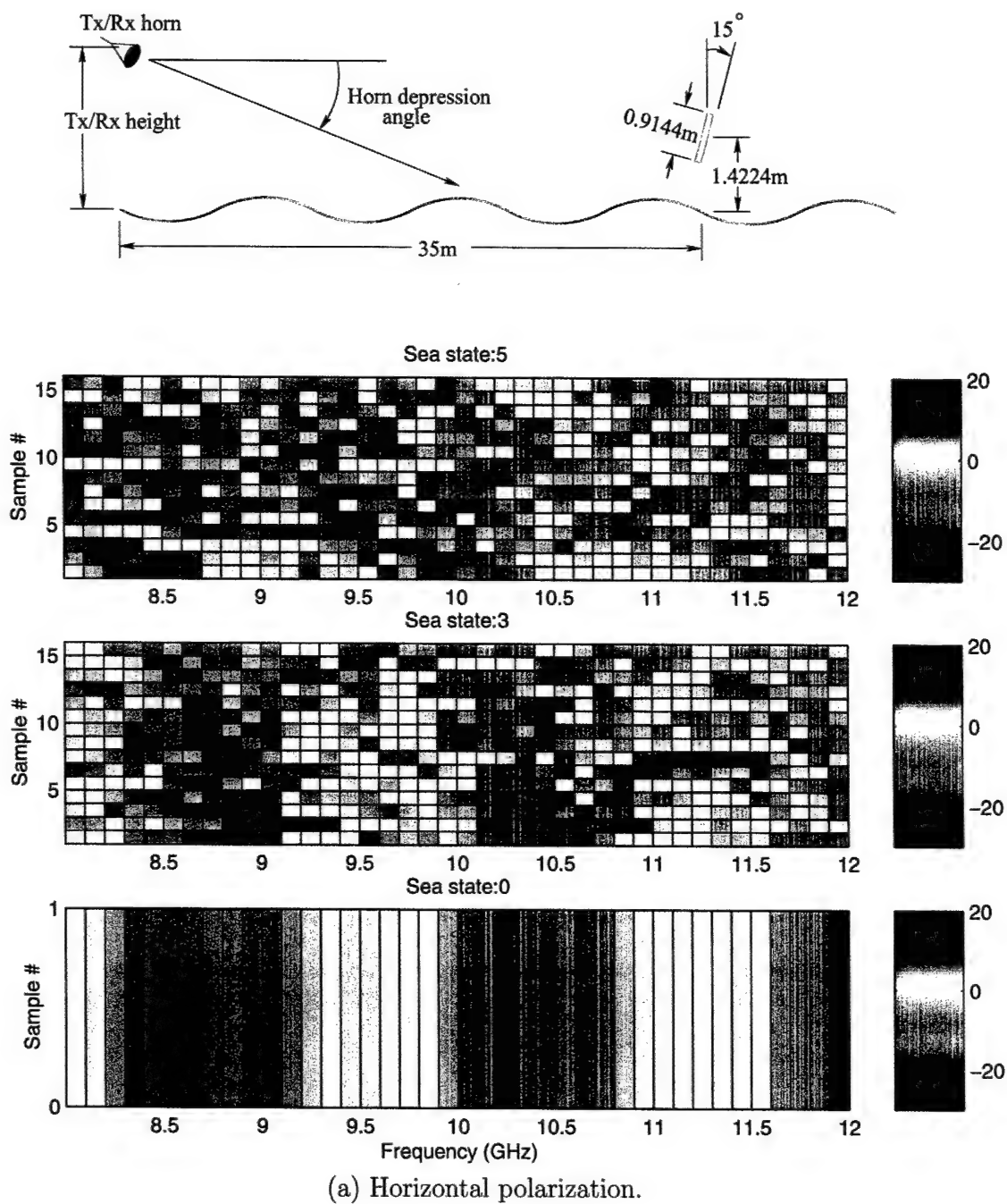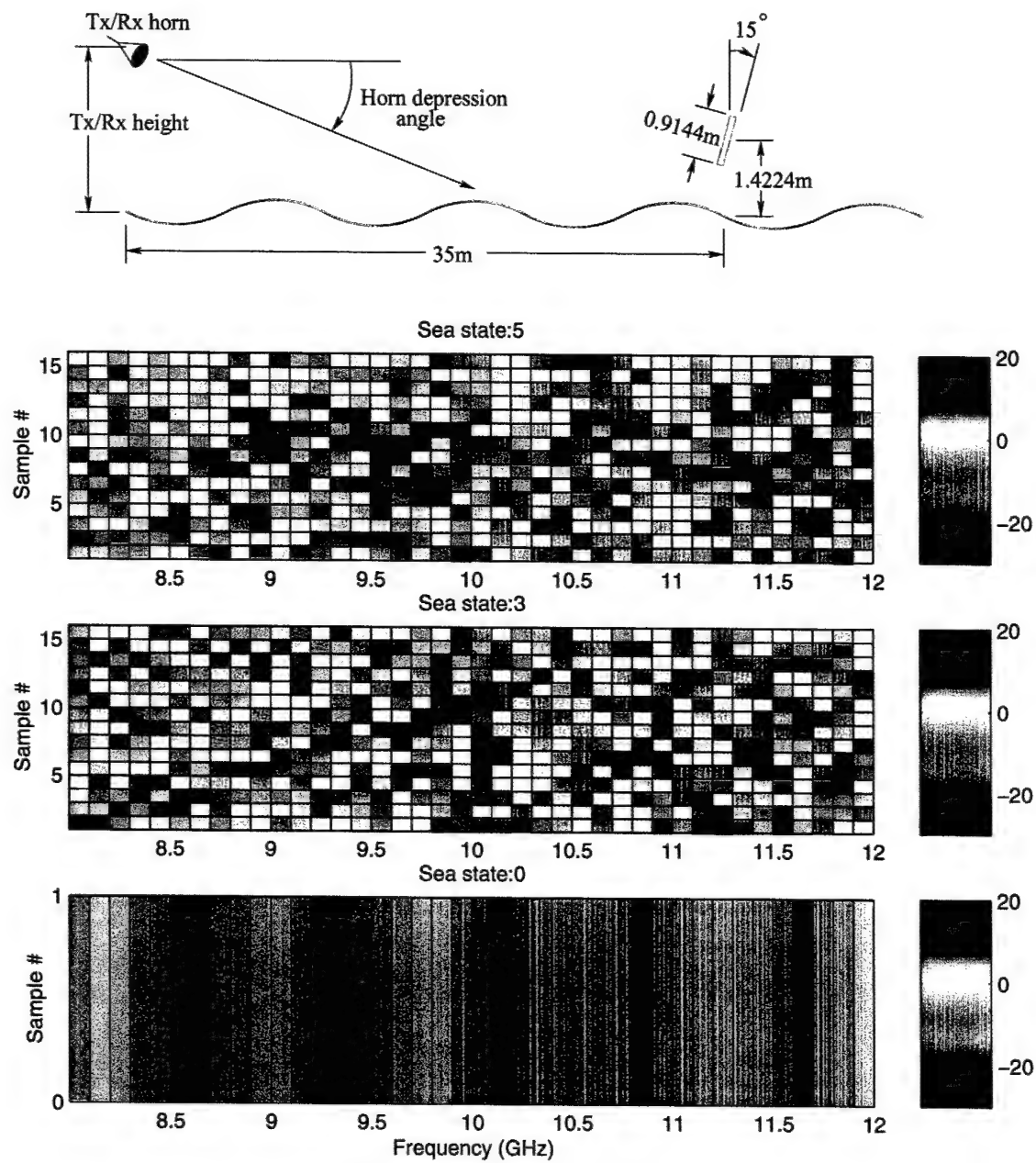(a) Coherent scattering, horizontal polarization.
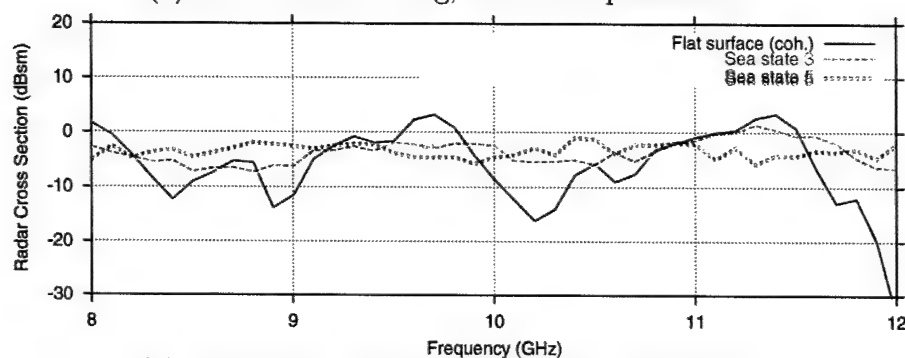


(b) Incoherent scattering, horizontal polarization.
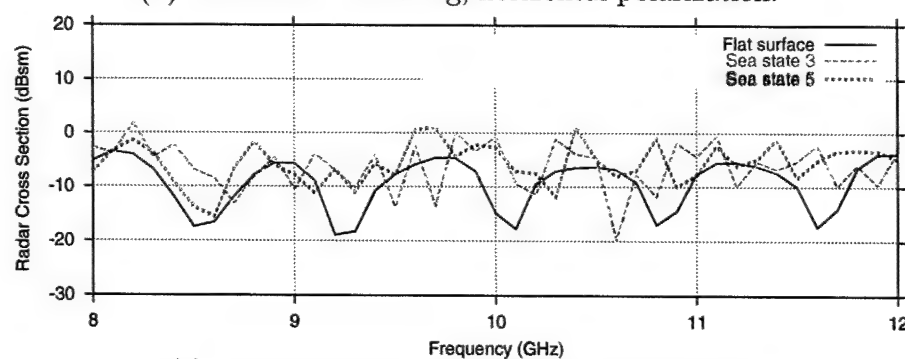


(c) Coherent scattering, vertical polarization.
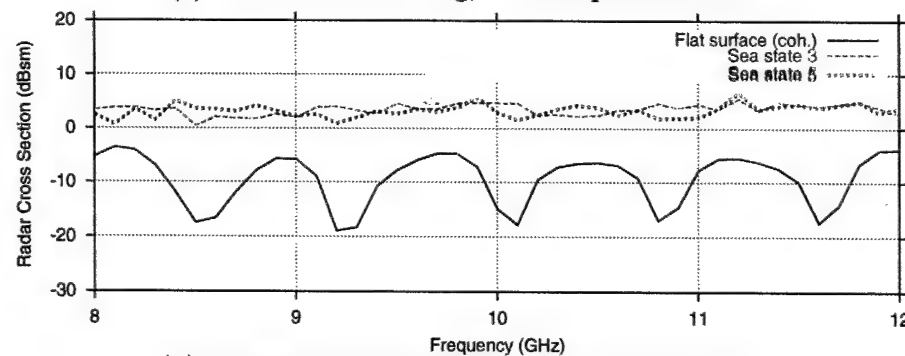


(d) Incoherent scattering, vertical polarization.

Figure 4.9: Coherent and incoherent backscattering for sea states 3 and 5. Target is a tilted flat plate. Tx/Rx height = 3.15 m, Horn depression angle = 9.9°.

51

## 4.2  3D Model using a Reduced-Order Iterative Physical Optics Method

As discussed in Section 1.2.1, the area of sea surface illuminated by the incident radar beam gives rise to an intractably large number of PO sample points. So instead of using the FBIPO method which includes all the surface-surface, surface-target, and target-target interactions, the reduced order IPO method is used which ignores the surface-surface interactions. Since the surface is much larger than the target, it is the surface-surface interactions that would dominate the required CPU time. Even with the reduced order IPO, each single realization took about 5 hours of CPU time on a 450 MHz Pentium II workstation.

The subtraction method described in Section 1.2 is used to remove the surface truncation effects from the backscatter simulations. However, this approach also removes the surface clutter contribution, which may be significant. As with the forward scatter simulations, only a few selected results will be shown here to compare the the GFB and reduced IPO results.

Figures 4.10 and 4.11 show the comparisons between reduced IPO and GFB for the vertical plate target. The analytic solution is also shown for the flat surface case. The agreement is good for the flat surface case, but only fair for the rough surfaces. This suggests that the reduced IPO is not sufficiently accurate for low-grazing angle rough surface scattering problems because the surface-to-surface interactions are ignored. A more efficient and accurate 3D solution is needed.
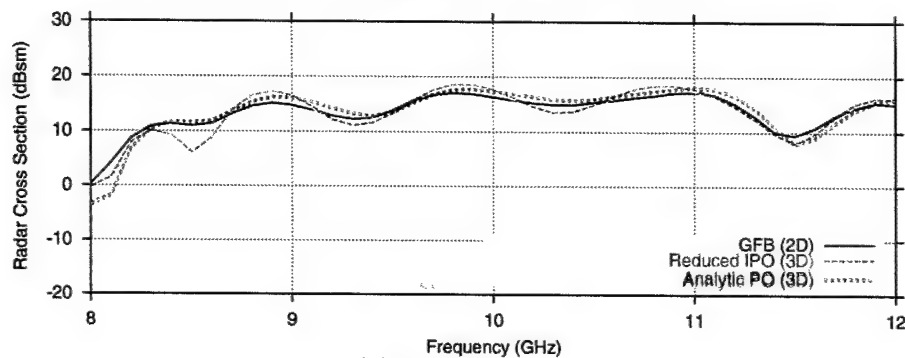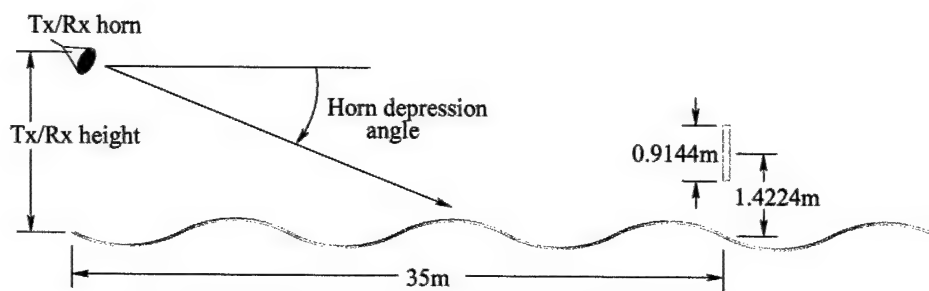
(a) Flat surface.
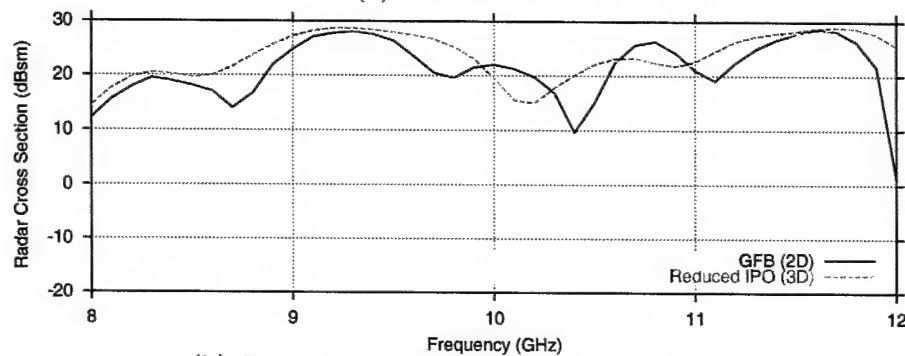
(b) Sea state 3, first Monte Carlo sample.
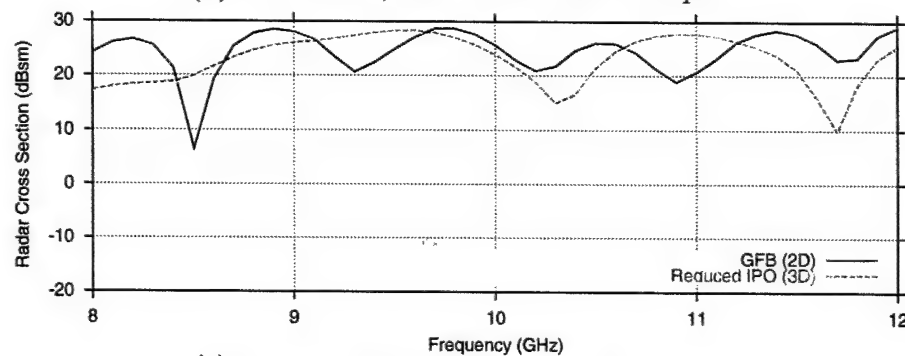
(c) Sea state 5, first Monte Carlo sample.

Figure 4.10: Reduced order PO and GFB comparisons of backscatter from a vertical plate, horizontal polarization. Tx height = 3.15 m, Horn depression angle 9.9°.

(a) Flat surface.

(b) Sea state 3, first Monte Carlo sample.

(c) Sea state 5, first Monte Carlo sample.
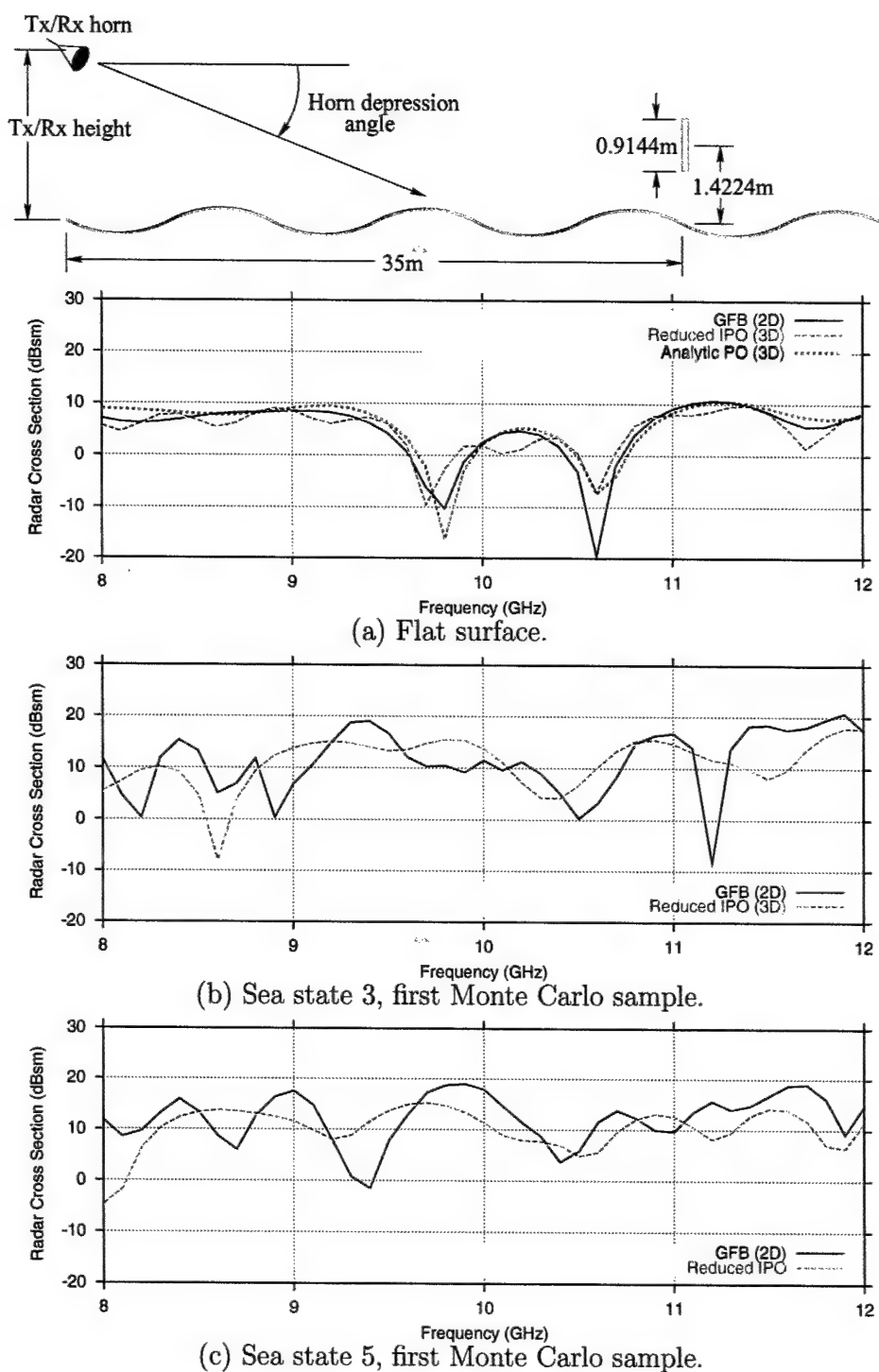
Figure 4.11: Reduced order PO and GFB comparisons of backscatter from a vertical plate, vertical polarization. Tx height = 3.15 m, Horn depression angle 9.9°.

54

# Chapter 5

# Summary and Future Work

## 5.1 Summary of Simulated Results

Simulated data has been presented to model the NSWC Carderock MASK radar scattering experiments. While the measured data has not yet been released, the comparisons between the GFB, reduced IPO, and analytic solutions lend confidence to the computer generated results. Furthermore, the coherent and incoherent scattering results processed from the Monte Carlo data show the expected trends, as did the surface clutter predictions. The relatively small number of Monte Carlo samples used here (sixteen) was checked for convergence, although more samples would give slightly better accuracy. Since it is not known how well the simulations model the actual experimental results, more Monte Carlo runs are not warranted at this time.

The forward scattering results showed that the forward scattered field is more incoherent for higher horn positions and higher sea states, as expected. In general, the vertical polarization results showed a weaker sea scattered signal due to the smaller sea surface reflection coefficient compared with horizontal polarization. The Brewster angle at X-band is around 5° in elevation, which is about in the middle of the range of angles considered in the forward scatter measurements.

The comparisons between GFB and first order PO for forward scattering showed that the PO solution gives only fair agreement for rough surfaces. Likewise, the reduced order IPO does not give very good agreement with GFB for backscatter from targets over rough

surfaces. This is most likely due to neglecting the surface-to-surface interactions which are responsible for correcting the shadowing of the incident radar beam by the ocean waves. The forward-backward IPO is expected to give much better agreement, but it is limited by the size of the surface illuminated by the incident radar beam. A more efficient and accurate 3D solution is needed.

The GFB backscatter simulations of the surface clutter (target absent) showed polarization-dependent clutter levels consistent with theory and measurements. The vertical polarization clutter is about 10 dB higher than horizontal. However, it is not known if the same clutter levels will be observed in the experiments because the hydrodynamic measurement of the ocean wave spectra was not sensitive enough to pick up the small scale roughness. Furthermore, the clutter component may be below the noise level in the measurements.

The backscatter results showed that the coherent RCS was reduced by the rough surface for the vertical plate target, and enhanced by the rough surface for the tilted plate. This may be significant for low-RCS targets such as the tilted flat plate. The RCS of the tilted flat plate was seen to be below the surface clutter level for vertical polarization. However, the coherent averaging over many Monte Carlo samples was able to discern the scattering from the target.

## 5.2   Future Work

For future work it remains to simulate the suspended sphere and floating squat cylinder targets. The cylinder floats on one of its flat sides, and is made of styrofoam so it moves freely on the large scale waves. The GFB codes would need to be modified to allow the target to change with each surface realization. However, since the target is not translationally invariant in the cross-direction, it may be difficult to convert the 2D RCS to 3D using the GFB codes. Since the squat cylinder target floats on the water, the FBIPO method could be applied because a much smaller area of the sea surface would need to be included in the model. The surface model used in the FBIPO code would also have to be modified to allow the target to move with the large waves.

It has been mentioned here that a new solution is needed that retains the accuracy and efficiency of the GFB method but is applicable to 3D targets. It therefore may be of interest to investigate a hybrid GFB/IPO model. In this approach the GFB (or FB) method would be used to find the fields over a 2D rough surface in the vicinity of the target. These fields would be used to illuminate a 3D target placed on a 3D translation of the same 2D rough surface. Then PO would give the induced currents on the target, and reciprocity would be used to compute the backscattered field as described in [1]. This approach would allow the efficiency and robustness of the 2D GFB solution to be applied to a realistic 3D geometry.

# Bibliography

[1] R.J. Burkholder, M.R. Pino, and D.-H. Kwon, "Development of Ray-Optical Methods for Studying the RCS of 2D Targets on a Rough Sea Surface," The Ohio State University ElectroScience Laboratory Technical Report 735231-1, January 1999.

[2] R.J. Burkholder, D. Colak, and H. Kiper, "Numerical Investigation of the RCS of 3D Targets on a Rough Sea Surface," The Ohio State University ElectroScience Laboratory Technical Report 735231-2, January 2000.

[3] R.J. Burkholder, P. Janpugdee and D. Colak, "Development of Computational Tools for Predicting the Radar Scattering from Targets on a Rough Sea Surface," The Ohio State University ElectroScience Laboratory Final Report 735231-3, January 2000.

[4] M.R. Pino, L. Landesa, J.L. Rodríguez, F. Obelleiro, and R.J. Burkholder, "The Generalized Forward-Backward Method for Analyzing the Scattering from Targets on Ocean–Like Rough Surfaces," IEEE Trans. Antennas and Propagation, Vol. 47, No. 6, pp. 961-969, June 1999.

[5] R.J. Burkholder, M.R. Pino, and F. Obelleiro, "A Monte Carlo Study of the Rough Sea Surface Influence on the Radar Scattering from 2D Ships," IEEE Antennas and Propagation Magazine, Vol. 43, No. 2, pp. 25-33, April 2001.

[6] F. Obelleiro, J.L. Rodriguez, and R.J. Burkholder, "An Iterative Physical Optics Approach for Analyzing the Electromagnetic Scattering by Large Open-Ended Cavities," IEEE Transactions on Antennas and Propagation, Vol. 43, No. 4, pp. 356-361, April 1995.

[7] R.J. Burkholder, "EM Scattering from a 3D Target on a Rough Sea Surface using Forward-Backward IPO," 2001 USNC/URSI National Radio Science Meeting, Boston, MA, July 8-13, 2001.

[8] P.H. Pathak and R.J. Burkholder, "High frequency scattering," Topic 1.5.2 in Scattering and Inverse Scattering in Pure and Applied Science, pp. 245-276, edited by E.R. Pike and P. Sabatier, Academic Press, Ltd., London, 2002.

[9] D. Holliday, L.L. DeRaad, and G.J. St-Cyr, "Forward-Backward: A new method for computing low-grazing angle scattering," *IEEE Trans. Antennas Propagat.*, vol. 44, pp. 722-729, May 1996.

[10] P. Tran, "Calculation of the scattering electromagnetic waves from a two-dimensional perfectly conducting surface using the method of ordered multiple interactions," *Waves in Random Media*, vol. 7, no. 3, pp. 295-302, July 1997.

[11] H.-T. Chou and J. T. Johnson, "Novel Acceleration algorithm for Forward-Backward method in the computation of scattering from rough surfaces," *Radio Science*, vol. 33, no. 5, pp. 1277–1287, 1998.

[12] M.R. Pino and F. Obelleiro, and R.J. Burkholder, "Spectral Acceleration of the Generalized Forward-Backward Method," *IEEE Trans. on Antennas and Propagation*, Vol. 50, No. 6, pp. 785-797, June 2002.

[13] R.J. Burkholder, "A Fast and Rapidly Convergent Iterative Physical Optics Algorithm for Computing the RCS of Open-Ended Cavities," *Applied Computational Electromagnetics Society Journal*, Vol. 16, No. 1, pp. 53-60, March 2001.

[14] W. J. Pierson and L. Moskowitz, "A proposed spectral form for fully developed wind seas based on the similarity theory of S.A. Kitaigorodskii," *J. Geophys. Res.*, vol. 69, pp. 5181–5190, 1964.

[15] M. Skolnik, *Radar Handbook*, McGraw-Hill, New York, 1990.

[16] R. F. Harrington, *Time-Harmonic Electromagnetic Fields*. McGraw-Hill, New York, 1961.

[17] M. Skolnik, *Introduction to Radar Systems*, Second Edition, McGraw-Hill, New York, 1980.

[18] L. Tsang, J. A. Kong, and R. T. Shin, *Theory of Microwave Remote Sensing*. Wiley, New York, 1985.